Research Square

Preprints are preliminary reports that have not undergone peer review.
They should not be considered conclusive, used to inform clinical practice,
or referenced by the media as validated information.

ACAT1 loss impairs TNFα-induced SOX4 accumulation and triggers lipid- dependent growth suppression in ERG-negative prostate cancer

Seho Park
Gwangju Institute of Science and Technology
Seungheon Shin
Gwangju Institute of Science and Technology
Seungwoo Seo
Gwangju Institute of Science and Technology
Jee-Young Han
Inha University Hospital
Doo Yong Chung
Inha University Hospital
Tae-Young Kim
Gwangju Institute of Science and Technology
Ki Woo Kim
Yonsei University College of Dentistry
Su-Geun Yang
Inha University College of Medicine
Steve K. Cho
scho@gist.ac.kr

Gwangju Institute of Science and Technology

Research Article

Keywords: Prostate cancer, ACAT1, AKT signaling, SOX4, TNFα, Lipid metabolism, PPARγ, ERG

Posted Date: November 12th, 2026

DOI: https://doi.org/10.21203/rs.3.rs-11476379/v1

License: This work is licensed under a Creative Commons Attribution 4.0 International License.
Read Full License

Additional Declarations: No competing interests reported.

ACAT1 loss impairs TNFα-induced SOX4 accumulation and triggers lipid-dependent growth suppression in ERG-negative prostate cancer

Seho Park[1], Seungheon Shin[2], Seungwoo Seo[3], Jee-Young Han[4], Doo Yong Chung[5], Tae-Young Kim[3], Ki Woo Kim[6], Su-Geun Yang[7] and Steve K. Cho[1,2]*

[1]Department of Life Sciences, Gwangju Institute of Science and Technology (GIST), Gwangju, Republic of Korea

[2]Department of Biomedical Science and Engineering, Gwangju Institute of Science and Technology (GIST), Gwangju, Republic of Korea

[3]Department of Environment and Energy Engineering, College of Engineering, Gwangju Institute of Science and Technology (GIST), Gwangju, Republic of Korea

[4]Department of Pathology, Inha University Hospital, Incheon, Republic of Korea

[5]Department of Urology, Inha University Hospital, Incheon, Republic of Korea

[6]Division of Physiology, Department of Oral Biology, BK21 FOUR, Yonsei University College of Dentistry, Seoul, Republic of Korea

[7]Department of Biomedical Science, BK21 FOUR program in Biomedical Science and Engineering, Inha University College of Medicine, Incheon, Republic of Korea

*Correspondence: Steve K. Cho, Department of Life Sciences, Gwangju Institute of Science and Technology (GIST), Gwangju 61005, Republic of Korea. Email: scho@gist.ac.kr

Abstract

Background

Prostate cancer progression involves metabolic reprogramming, but whether these changes differ according to ERG status remains unclear. This study aimed to characterize ERG-associated metabolic patterns during progression to metastatic castration-resistant prostate cancer (mCRPC) and to identify and functionally validate genes contributing to these features.

Methods

ERG-stratified bulk transcriptomic analyses were integrated with single-cell analyses to examine relationships between progression-associated tumor cell states and metabolic programs in ERG-negative prostate cancer and to prioritize candidate genes. Acetyl-CoA acetyltransferase 1 (ACAT1) was depleted in two ERG-negative prostate cancer cell lines, PC3 and C4-2B, to assess progression-related phenotypes and SOX4 protein regulation. Human prostate cancer tissues were examined for spatial relationships between ACAT1 and SOX4. Metabolomic and lipidomic profiling, extracellular lipid restriction, and PPARγ antagonism were used to investigate metabolic remodeling and its functional consequences.

Results

Integrated transcriptomic analyses revealed progression-associated suppression of metabolic programs in ERG-negative prostate cancer and identified a stemness-associated, epithelial–mesenchymal transition (EMT)-like, androgen receptor (AR)-low tumor cell state with elevated ACAT1 expression. ACAT1 depletion suppressed proliferation, anchorage-independent growth, and gap closure, reduced AKT phosphorylation, increased p27 abundance, and induced a senescence-associated phenotype. Basal SOX4 protein abundance decreased without a corresponding reduction in SOX4 mRNA, and proteasome inhibition restored SOX4 abundance. ACAT1 loss also prevented TNFα-induced SOX4 accumulation. Human prostate

cancer specimens showed focal spatial overlap between ACAT1-positive regions and a subset of extranuclear SOX4 signals. ACAT1 loss induced broad metabolomic and lipidomic remodeling and neutral lipid accumulation without significantly altering palmitate oxidation. Extracellular lipid restriction attenuated lipid accumulation and alleviated the proliferative and AKT–p27 signaling defects. ACAT1 depletion increased PPARγ abundance, and the PPARγ antagonist GW9662 reduced lipid accumulation and alleviated these defects in ACAT1-knockout PC3 cells.

Conclusions

ACAT1 maintains basal and TNFα-induced SOX4 protein abundance and supports lipid homeostasis in ERG-negative prostate cancer cells. Its loss induces metabolic remodeling and extracellular lipid-dependent proliferative suppression. Rescue by lipid restriction and PPARγ antagonism supports a functional contribution of the lipid response to growth suppression.

Keywords

Prostate cancer, ACAT1, AKT signaling, SOX4, TNFα, Lipid metabolism, PPARγ, ERG

Background

Prostate cancer encompasses a broad disease spectrum ranging from localized, androgen-dependent tumors to recurrent, metastatic, and castration-resistant disease [1]. Although localized tumors can often be controlled by surgery or radiotherapy, advanced prostate cancer adapts to androgen deprivation and other therapeutic pressures, ultimately progressing to metastatic castration-resistant prostate cancer (mCRPC) [1]. This progression involves extensive molecular and cellular adaptation that enables continued tumor growth and survival [1].

Metabolic reprogramming is an integral component of this adaptive process. During progression, prostate cancer cells alter nutrient utilization, mitochondrial activity, lipid handling, and energy production to accommodate changing bioenergetic and biosynthetic demands [2–4]. These metabolic changes have generally been examined in relation to disease stage or treatment resistance. However, prostate cancer is composed of molecularly distinct subgroups, and the metabolic adaptations accompanying progression may differ according to the underlying molecular context.

One of the major molecular subdivisions of prostate cancer is defined by ERG, an ETS-family transcription factor frequently activated through the TMPRSS2–ERG genomic fusion [5,6]. ERG-positive and ERG-negative tumors differ in their genomic architecture, transcriptional programs, and tumor-associated epithelial cell states [6,7]. These differences suggest that the metabolic adaptations required for progression may also follow ERG-defined patterns. Analyses that combine ERG-positive and ERG-negative tumors could therefore obscure metabolic changes that arise preferentially within either subgroup.

To determine whether progression-associated metabolic reprogramming differs according to ERG status, we performed an ERG-stratified transcriptomic analysis of primary prostate cancer

and mCRPC. The metabolic pathway changes accompanying progression were distinct between ERG-positive and ERG-negative disease, with ERG-negative progression exhibiting broader suppression of metabolic programs. Single-cell transcriptomic analysis further resolved the tumor cell states associated with this metabolic pattern. Together, these findings established ERG status as a relevant framework for investigating metabolic reprogramming during prostate cancer progression and provided a basis for identifying molecular factors associated with the ERG-negative metabolic phenotype.

Integrative analysis highlighted acetyl-CoA acetyltransferase 1 (ACAT1) as a candidate metabolic factor associated with ERG-negative progression. ACAT1 is a mitochondrial thiolase involved in acetyl-CoA and ketone body metabolism [8]. Previous proteomic and tissue-based studies have reported increased ACAT1 abundance in high-grade, metastatic, and castration-resistant prostate cancer [9–11]. Notably, ACAT1 expression independently predicted biochemical recurrence specifically in ERG-negative disease [10]. Functional studies have also implicated ACAT1 in prostate cancer cell proliferation, migration, invasion, tumor growth, and survival during therapeutic stress [12–15]. Despite these observations, whether ACAT1 contributes functionally to the metabolic reprogramming and aggressive phenotype of ERG-negative prostate cancer remains unresolved. This study therefore investigated the metabolic and cellular consequences of ACAT1 loss in ERG-negative prostate cancer models.

Methods

Cell culture and generation of stable cell populations

PC3, Du145, and C4-2B cells were cultured in RPMI 1640 medium containing L-glutamine, whereas HEK293T cells were maintained in high-glucose Dulbecco's modified Eagle medium. Both media were supplemented with 100 IU/mL penicillin, 100 μg/mL streptomycin, and 10% fetal bovine serum. Cells were maintained at 37°C in a humidified atmosphere containing 5% CO_2 and confirmed to be mycoplasma-free. Cells were treated with TNFα, MG132, chloroquine (CQ), C6-ceramide (d18:1/6:0), or GW9662, as indicated. Cell lines, reagents, antibodies, plasmids, and oligonucleotide sequences are listed in the supplementary materials table.

For shRNA-mediated depletion, synthesized oligonucleotides targeting ACAT1 (shACAT1) or SOX4 (shSOX4), or containing the control sequence (shCTRL), were inserted into the pLKO.1 vector. Lentiviral particles were produced by cotransfecting the resulting pLKO.1 constructs with pMD2.G and psPAX2 into HEK293T cells using FuGENE HD Transfection Reagent. At 48 h after transfection, lentiviral supernatants were collected and used to transduce the indicated target cells in the presence of polybrene. Transduced cells were selected with 2 μg/mL puromycin.

For ACAT1 knockout, PC3 cells were cotransfected with an ACAT1-targeting CRISPR–Cas9 plasmid and the corresponding homology-directed repair plasmid using FuGENE HD Transfection Reagent. PC3 cells transfected with a non-targeting control CRISPR–Cas9 plasmid and subjected to the same culture and selection procedure were used as controls. At 24–48 h after transfection, cells were selected with 2 μg/mL puromycin, and ACAT1 loss was validated by immunoblotting.

All stable knockdown and knockout experiments were performed using puromycin-selected

polyclonal cell populations rather than single-cell-derived clones.

RNA extraction and quantitative reverse transcription PCR

Total RNA was extracted using TRIzol reagent and a Direct-zol RNA Miniprep Kit, including DNase treatment. RNA concentrations were measured using a NanoDrop spectrophotometer. Equal amounts of total RNA were used for first-strand cDNA synthesis using TOPscript RT DryMIX (dT18 plus). Each quantitative PCR reaction contained cDNA corresponding to 20 ng of input total RNA. Quantitative PCR was performed using TOPreal qPCR 2X PreMIX (SYBR Green with low ROX, UDG plus) on a 7500 Real-Time PCR System. Threshold cycle (Ct) values were determined using the instrument software. Relative mRNA expression was normalized to ACTB or 18S rRNA and calculated using the 2^−ΔΔCt method.

Protein extraction and immunoblotting

Harvested cells were lysed in RIPA buffer supplemented with protease and phosphatase inhibitors for 30 min at 4°C. Cell lysates were centrifuged at 16,000 × g for 15 min, and the supernatants were collected. Protein concentrations were determined using Bradford reagent. Equal amounts of protein (20 μg) were separated by SDS–PAGE and transferred onto nitrocellulose membranes. Membranes were blocked with 5% bovine serum albumin for 1 h and incubated overnight at 4°C with primary antibodies diluted in TBS-T containing 0.1% Tween 20. After washing with TBS-T, membranes were incubated with secondary antibodies diluted in TBS-T for 1 h at room temperature. Membranes were washed twice with TBS-T, and protein signals were detected using Amersham ECL Prime Western Blotting Detection Reagent. Band intensities were quantified using Image Lab software or, for images acquired using Fuji Medical X-Ray Film, Fiji/ImageJ. Target protein band intensities were normalized to the corresponding loading control, and relative values were calculated by setting the indicated control condition to 1.

Cell proliferation assay

Cells were seeded in 6-well plates at the indicated density. Total cell numbers were counted using a hemocytometer every 24 h for 96 h after seeding. For delipidated-serum experiments, cells were cultured in medium supplemented with delipidated FBS prepared using a previously described lipid-stripping protocol [16].

Anchorage-independent growth assay

One hundred cells were embedded in 0.35% soft agar prepared in 1× RPMI 1640 and layered over a base layer of 0.7% soft agar prepared in 1× RPMI 1640. PC3 and C4-2B cells were cultured for 21 and 28 days, respectively. Images were acquired at ×40 magnification, and colonies exceeding 50 μm in diameter were counted manually.

Wound-healing assay

Cells were seeded in 12-well plates at a density of 2.0×10^5 cells/well and incubated overnight at 37°C with 5% CO_2. The cell monolayer was scratched using a 200-μL pipette tip, and images were acquired at 0 and 24 h using a microscope at ×4 magnification. Wound areas were measured using ImageJ software. Gap closure was calculated as the reduction in wound area between 0 and 24 h and expressed relative to the corresponding control.

Senescence-associated β-galactosidase staining

Senescence-associated β-galactosidase staining was performed using a Senescence β-Galactosidase Staining Kit. Cells were washed with PBS and fixed with 1× fixative solution for 10–15 min at room temperature. After washing twice with PBS, cells were incubated with freshly prepared β-galactosidase staining solution containing X-gal at pH 6.0 overnight at 37°C in a dry incubator without CO_2. Blue-stained senescence-associated β-galactosidase-positive cells were visualized under a light microscope. In parallel, cells from matched plates were lysed, and lamin B1 abundance was assessed by immunoblotting as an additional marker of cellular

171 senescence.

172 **CE–TOFMS-based metabolite profiling**

173 Metabolite profiling was performed in triplicate using control and ACAT1-knockout PC3 cells
174 by capillary electrophoresis–time-of-flight mass spectrometry (CE–TOFMS) at Human
175 Metabolome Technologies, Inc., according to the company's standard protocol. After removal
176 of the culture medium, cells were washed twice with 5% mannitol solution, treated with 800
177 μL of methanol, and incubated at room temperature for 30 s. The methanol extract was mixed
178 with 550 μL of internal standard solution diluted in HPLC-grade water. One milliliter of the
179 metabolite extract was transferred to a new tube and centrifuged at 2,300 × g for 5 min at 4°C.
180 A total of 700 μL of the resulting supernatant was filtered through an Ultrafree-MC centrifugal
181 filter at 9,100 × g for 120 min at 4°C to remove proteins. The filtrate was dried using a
182 centrifugal evaporator before CE–TOFMS analysis.

183 **Lipid extraction and LC–MS/MS lipidomic analysis**

184 Total lipids were extracted from cell pellets containing 3.0×10^6 cells using a modified Folch
185 method [17]. Briefly, cell pellets were extracted with chloroform/methanol (2:1, v/v), and the
186 resulting lipid-containing supernatants were collected and dried in a vacuum concentrator
187 before LC–MS/MS analysis.

188 LC–MS/MS was performed using an Agilent 1290 UPLC system coupled to an Agilent 6546
189 quadrupole time-of-flight mass spectrometer equipped with an electrospray ionization source.
190 Chromatographic separation was adapted from the method of Bishop and Fiehn [18] and
191 performed using a Waters Acquity UPLC BEH C18 column (2.1 × 100 mm, 1.7 μm) maintained
192 at 65°C, with an injection volume of 3 μL and a flow rate of 0.6 mL/min. Mobile phases A and
193 B consisted of acetonitrile/water (60:40, v/v) and isopropanol/acetonitrile (90:10, v/v),
194 respectively. Both mobile phases contained 10 mM ammonium formate for positive-ion

analysis or 10 mM ammonium acetate for negative-ion analysis. The gradient profiles for both ionization modes followed those described by Bishop and Fiehn [18]. Data were acquired over an m/z range of 100–3000 using data-dependent MS/MS acquisition, with the four most abundant precursor ions selected per cycle. Collision energies were set to 20 and 40 V for positive- and negative-ion modes, respectively.

Lipid features were processed and annotated using Lipid Annotator [19]. Lipid abundances were normalized to cell counts and statistically analyzed using MetaboAnalyst [20]. Lipid ontology enrichment analysis was performed using LION/web [21].

Oil Red O staining and quantification

Cells were washed with PBS, fixed with 10% formalin, and incubated with 60% isopropanol for 5 min. After drying, cells were stained for 20 min at room temperature with Oil Red O working solution prepared by mixing a 0.35% Oil Red O stock solution in isopropanol with distilled water at a 3:2 ratio. Cells were then washed with distilled water and imaged under a microscope. For quantification, Oil Red O dye was eluted with 100% isopropanol for 10 min. Absorbance was measured at 500 nm and normalized to the cell number determined from parallel plates.

Fatty acid β-oxidation assay

Fatty acid β-oxidation was measured using [9,10-^{3}H(N)]palmitic acid. Cells were seeded at 5.0 × 10^{4} cells/well in 24-well plates and incubated overnight. Cells were pretreated for 1 h with 100 μM palmitic acid and 1 mM carnitine in serum-free, low-glucose medium containing 5 mM glucose. The medium was then replaced with serum-free, low-glucose medium containing 1 μCi [9,10-^{3}H(N)]palmitic acid and 1 mM carnitine, and cells were incubated for 3 h at 37°C with 5% CO_2. Etomoxir (10 μM) was included as an inhibitor control for carnitine palmitoyltransferase 1 (CPT1).

To terminate the reaction, 450 µL of incubation medium was mixed with 450 µL of 10% trichloroacetic acid and centrifuged at 4,000 × g for 10 min. A total of 850 µL of the supernatant was neutralized with 90 µL of 6 M NaOH. Unmetabolized radiolabeled palmitate was removed using an AmberChrom 1X2 ion-exchange column. Water-soluble metabolites were eluted twice with 800 µL of sterile water, mixed with 4 mL of Ultima Gold LLT scintillation cocktail, and analyzed using a Hidex 300 SL liquid scintillation counter.

Cell viability and C6-ceramide dose-response assay

PC3 and C4-2B cells were seeded at 5.0×10^3 and 1.0×10^4 cells/well, respectively, and incubated for 48 h to allow cell attachment. Cells were then treated with the indicated concentrations of C6-ceramide for 24 h. After removal of the culture medium, 15 µL of MTS reagent was added, and cells were incubated for 45 min. Absorbance was measured at 492 nm and normalized to that of untreated cells to generate C6-ceramide dose-response curves.

Gelatin zymography

Cells were washed and incubated in serum-free medium for 24 h, after which conditioned media were collected. Equal volumes of conditioned media were mixed with non-reducing sample buffer without heating and separated on 7.5% polyacrylamide gels containing gelatin. After electrophoresis, gels were washed twice for 30 min in washing buffer containing 2.5% Triton X-100, 50 mM Tris-HCl (pH 7.5), 5 mM $CaCl_2$, and 1 µM $ZnCl_2$. Gels were then incubated for 24 h at 37°C in incubation buffer containing 1% Triton X-100, 50 mM Tris-HCl (pH 7.5), 5 mM $CaCl_2$, and 1 µM $ZnCl_2$. Gels were stained with Coomassie Brilliant Blue and destained until gelatinolytic activity was visible as clear bands against a blue background.

After collection of the conditioned media, the remaining cells were harvested using trypsin and lysed, and total cellular protein concentrations were determined. Gelatinolytic band intensities were normalized to the corresponding cellular protein concentrations. Equal volumes of the

same conditioned media were also subjected to immunoblotting to assess MMP9 abundance.

Immunofluorescence analysis of human prostate cancer tissues

Human prostate cancer tissues obtained from Inha University Hospital were prepared as formalin-fixed paraffin-embedded sections. Tissue sections were deparaffinized in xylene and rehydrated through graded ethanol solutions. Heat-induced antigen retrieval was performed in 10 mM sodium citrate buffer at 110°C for 10 min. Tissues were permeabilized with 0.1% Triton X-100 for 5 min and blocked with goat serum for 1 h. Samples were incubated overnight at 4°C with primary antibodies against ACAT1 and SOX4, followed by incubation for 1 h at room temperature in the dark with Alexa Fluor 488-conjugated goat anti-rabbit IgG and Alexa Fluor 594-conjugated goat anti-mouse IgG, each diluted 1:500. Nuclei were counterstained with Hoechst, and fluorescence images were acquired using a confocal microscope. Fluorescence intensity profiles were generated using Fiji, and colocalization of ACAT1 and SOX4 signals was evaluated by calculating Pearson correlation coefficients using the Coloc 2 plugin.

Transcriptomic and clinical analyses

Transcriptomic analyses were performed using R version 4.3.3 [22]. For GSE32269 [23], samples were classified as primary prostate cancer or metastatic castration-resistant prostate cancer (mCRPC) and as ERG fusion-positive or ERG fusion-negative according to the accompanying sample metadata. Gene set enrichment analysis (GSEA) was performed using clusterProfiler (version 4.10.1) [24] to compare primary and mCRPC samples within the ERG fusion-positive and ERG fusion-negative subgroups using Kyoto Encyclopedia of Genes and Genomes (KEGG) pathway gene sets.

For GSE176031 [7], cells annotated as ERG-negative cancer cells by the original authors were selected and analyzed using Seurat (version 5.2.1) [25]. The subset was scaled, and principal component analysis was performed using 100 principal components. UMAP dimensionality

reduction and nearest-neighbor graph construction were performed using principal components 1–100, followed by clustering at a resolution of 0.5. Marker genes for the selected cluster were identified relative to all remaining cells using FindMarkers with the receiver operating characteristic test, a log-fold-change threshold of 0.25, and selection of positive markers only. Single-sample gene set enrichment analysis (ssGSEA) was performed on the normalized RNA expression matrix using the GSVA package (version 1.50.5) [26]. The 'WANG PROSTATE CANCER ANDROGEN INDEPENDENT [27]', 'OUYANG PROSTATE CANCER PROGRESSION UP' [28], 'AKT UP V1 UP' [29], and 'HALLMARK TNFA SIGNALING VIA NFKB' gene sets obtained from the Molecular Signatures Database (MSigDB) [30] were used to evaluate transcriptional states associated with prostate cancer progression. Median ssGSEA scores were calculated for each cluster and standardized as Z-scores. For each gene set, scores for cells in each cluster were compared with those for all remaining cells using the Wilcoxon rank-sum test. Overall survival in the TCGA prostate adenocarcinoma cohort (TCGA-PRAD) [6] was analyzed using GEPIA2 [31].

Statistical analysis

Statistical analyses of experimental data were performed using GraphPad Prism. Unless otherwise indicated, quantitative data are presented as the mean ± standard deviation (SD). Comparisons between two independent groups were performed using unpaired two-tailed t-tests. Experiments involving two independent variables were analyzed using ordinary two-way ANOVA followed by Šídák's multiple-comparisons test with a single pooled variance. $P < 0.05$ was considered statistically significant.

Use of large language models

During manuscript preparation, the authors used ChatGPT (OpenAI) for English-language editing, stylistic refinement, and assistance in improving manuscript clarity and organization.

All scientific interpretations, conclusions, and final wording were critically reviewed and approved by the authors, who take full responsibility for the manuscript.

Results

Integrated transcriptomic analyses identify ACAT1 within a progression-associated ERG-negative prostate cancer cell state

To identify metabolism-related transcriptional programs associated with prostate cancer progression, we performed gene set enrichment analysis (GSEA) using gene-expression microarray data from the GSE32269 cohort, which includes TMPRSS2–ERG fusion-positive and fusion-negative primary prostate cancer (PCa) and metastatic castration-resistant prostate cancer (mCRPC) samples [23]. The analyzed cohort comprised ERG-positive primary PCa (n = 12), ERG-positive mCRPC (n = 11), ERG-negative primary PCa (n = 10), and ERG-negative mCRPC (n = 18). Comparative GSEA identified two KEGG gene sets that met the significance criteria exclusively in the ERG-positive comparison, five that met the criteria in both ERG subgroups, and seven that met the criteria exclusively in the ERG-negative comparison (Fig. 1A, Supplementary Figure 1A–C, and Supplementary Table S1). All seven gene sets identified exclusively in the ERG-negative comparison were related to metabolic processes and exhibited negative normalized enrichment scores in the mCRPC-versus-primary comparison, indicating relative enrichment in primary tumors and attenuation during progression to mCRPC.

To determine whether a similar metabolism-low state was detectable within ERG-negative primary tumors, we analyzed single-cell RNA-sequencing (scRNA-seq) data from the GSE176031 cohort using the authors' annotation of ERG-negative cancer cells [7]. Unsupervised clustering of ERG-negative tumor cells from 11 patients identified nine transcriptionally distinct clusters, as visualized by UMAP (Fig. 1B, left). Among these, Cluster 5 showed relatively high expression of the stemness-associated transcription factors KLF2 and SOX4 and the mesenchymal marker VIM, together with relatively low expression of the epithelial marker CDH1 and AR (Fig. 1B, right). These features were consistent with a

stemness-associated, EMT-like, and relatively AR-low transcriptional state.

Single-sample gene set enrichment analysis (ssGSEA) showed that Cluster 5 had relatively high scores for prostate cancer progression, AKT1-driven prostate cancer, TNFα signaling via NF-κB, and AR-independent signatures, together with low scores for several metabolism-related gene sets, including fatty acid, tyrosine, and histidine metabolism (Fig. 1C, left, Supplementary Table S2). Across the nine cluster-level transcriptional profiles, the prostate cancer progression signature score correlated positively with the AKT1-driven prostate cancer, TNFα signaling via NF-κB, and AR-independent signature scores. Among the seven metabolic gene sets examined, fatty acid, histidine, and tyrosine metabolism showed significant inverse correlations with the progression signature (Fig. 1C right, Supplementary Table S2). Cluster 5 therefore occupied the progression-high, metabolism-low end of these cluster-level transcriptional relationships.

Together with the negative enrichment of these metabolic gene sets in the ERG-negative mCRPC-versus-primary comparison, these findings indicate that reduced transcriptional activity of fatty acid, histidine, and tyrosine metabolic programs is associated with ERG-negative metastatic progression and is detectable within a progression-associated tumor cell state in primary PCa.

We next integrated single-cell, bulk transcriptomic, and clinical outcome data to prioritize candidate genes associated with this tumor cell state (Fig. 1D). Genes enriched in Cluster 5 relative to the other clusters in GSE176031 were selected using the criteria area under the curve (AUC) > 0.6, average log2 fold change > 0.5, and expression in ≥ 50% of Cluster 5 cells. To prioritize genes showing an ERG-negative-biased progression pattern, we further required a positive log fold change and $P < 0.05$ in the ERG-negative mCRPC-versus-primary comparison, together with $P > 0.1$ in the corresponding ERG-positive comparison. This intersection yielded

19 candidate genes (Fig. 1D and Supplementary Table S3). Exploratory median-split overall survival analysis of these candidates in the TCGA-PRAD cohort [6] identified RPL35A and ACAT1 as the only genes with log-rank $P < 0.05$ (Supplementary Table S3). Among these candidates, ACAT1 was prioritized because it encodes a metabolic enzyme and because its association with disease recurrence was previously reported in ERG-negative, but not ERG-positive, PCa [10], consistent with the disease context identified by our transcriptomic analyses. ACAT1 expression was relatively high in Cluster 5 compared with the other ERG-negative tumor cell clusters in GSE176031 (Fig. 1E). In GSE32269, ACAT1 mRNA expression was significantly higher in ERG-negative mCRPC than in ERG-negative primary tumors ($P = 0.0382$), whereas no significant difference was observed between ERG-positive primary PCa and mCRPC ($P = 0.3384$) (Fig. 1F). In the TCGA-PRAD cohort, median-based stratification showed that high ACAT1 expression was associated with shorter overall survival (high: $n = 246$, low: $n = 246$, log-rank $P = 0.047$, Fig. 1G). ACAT1 expression also correlated positively with the Cluster 5 signature ssGSEA score across 492 TCGA-PRAD tumors (Spearman correlation $r = 0.4137$, $P < 0.0001$) (Fig. 1H). Collectively, these multi-cohort analyses prioritized ACAT1 as a metabolism-related candidate associated with the progression-related Cluster 5 state and elevated in the ERG-negative mCRPC-versus-primary comparison, supporting its subsequent functional investigation.

ACAT1 is required to maintain proliferative and aggressive phenotypes in ERG-negative prostate cancer cells

To investigate the functional role of ACAT1 in ERG-negative PCa, we first examined ERG mRNA expression in PC3, C4-2B, and Du145 cells. ERG mRNA was detectable in Du145 cells but not in PC3 or C4-2B cells under our assay conditions (Supplementary Figure 2A). We therefore selected PC3 and C4-2B as ERG-negative models and generated ACAT1-knockout

PC3 cells using CRISPR/Cas9 and stable ACAT1-knockdown C4-2B cells using shRNA. ACAT1 depletion was confirmed by immunoblotting (Supplementary Figure 2B). In both models, ACAT1 depletion significantly reduced cell proliferation over 96 h (Fig. 2A) and impaired anchorage-independent growth, as shown by a marked reduction in the number of soft agar colonies exceeding 50 μm in diameter (Fig. 2B). ACAT1-depleted cells also exhibited significantly reduced gap closure over 24 h in wound-healing assays (Fig. 2C).

At the molecular level, ACAT1 depletion reduced AKT phosphorylation at Ser473, a key regulatory modification associated with full AKT activation [32,33], and increased p27 protein abundance in both models (Fig. 2D). These reciprocal changes were consistent with suppression of the AKT–p27 signaling axis [34]. The attenuation of AKT signaling following ACAT1 depletion was also concordant with the high ACAT1 expression and elevated AKT1-driven prostate cancer signature score observed in the progression-associated Cluster 5 state identified by scRNA-seq (Fig. 1C, E). This growth-suppressive response was further accompanied by increased senescence-associated β-galactosidase (SA-β-gal) staining (Fig. 2E) and reduced lamin B1 protein abundance (Fig. 2F), consistent with acquisition of a senescence-associated phenotype [35].

To determine whether this dependency was shared across PCa cellular contexts, we next depleted ACAT1 in Du145 cells, in which ERG mRNA was detectable (Supplementary Figure 2A). In contrast to its effects in PC3 and C4-2B cells, ACAT1 depletion in Du145 cells did not reduce AKT phosphorylation at Ser473 or increase p27 protein abundance (Supplementary Figure 2C) and did not significantly alter proliferation or gap closure (Supplementary Figure 2D, E). Moreover, ACAT1 depletion produced neither an apparent increase in SA-β-gal staining nor a reduction in lamin B1 abundance in Du145 cells (Supplementary Figure 2F, G).

ACAT1 is required for TNFα-induced SOX4 accumulation

Because Cluster 5 displayed elevated TNFα signaling via NF-κB and AKT signature scores together with high SOX4 expression, we next examined whether ACAT1 contributed to TNFα-responsive signaling. Previous studies have shown that TNFα induces RelA phosphorylation, promotes post-transcriptional stabilization of SOX4 protein through a proteasome-sensitive mechanism, and enables RelA and SOX4 to function as transcriptional partners in selected cellular contexts [36–38] (Fig. 3A).

In PC3 cells, ACAT1 loss reduced basal RelA phosphorylation at Ser536, a regulatory site within the RelA transactivation domain that has been linked to its transcriptional activity [39,40] (Fig. 3B). Given this reduction in RelA phosphorylation and the impaired gap closure observed following ACAT1 loss, we next examined MMP9, an NF-κB-regulated protease linked to prostate cancer cell migration and invasion [41,42]. ACAT1 loss decreased cellular and conditioned-medium MMP9 abundance and reduced MMP9 gelatinolytic activity, whereas MMP2 activity was not significantly altered (Supplementary Figure 3A, B). TNFα induced RelA phosphorylation in both control and ACAT1-knockout PC3 cells, but the response was attenuated following ACAT1 loss (Supplementary Figure 3C). In C4-2B cells, basal phosphorylated RelA was barely detectable. TNFα induced RelA phosphorylation in both control and ACAT1-depleted cells, with no apparent attenuation following ACAT1 depletion (Fig. 3C). Thus, the effect of ACAT1 loss on basal and TNFα-responsive RelA signaling was cell context-dependent.

Next, we examined the TNFα–SOX4 axis. ACAT1 depletion did not significantly alter SOX4 mRNA expression in either PC3 or C4-2B cells (Fig. 3D) but markedly reduced SOX4 protein abundance in both models (Fig. 3E). This RNA–protein discordance suggested that ACAT1 maintains SOX4 abundance through a post-transcriptional process shared across the two ERG-negative models. To determine whether protein degradation contributed to the reduction in

SOX4 abundance, we treated cells with the proteasome inhibitor MG132 or the lysosomal inhibitor chloroquine. MG132 increased SOX4 abundance in both control and ACAT1-depleted cells, bringing SOX4 abundance to similar levels between the two groups in both models (Fig. 3F). In contrast, chloroquine produced no evident restoration of SOX4 in PC3 cells but increased SOX4 abundance in C4-2B cells, suggesting a cell context-dependent contribution of lysosome-sensitive regulation (Fig. 3F). The shared response to MG132 nevertheless implicated a proteasome-sensitive process as a common component of ACAT1-dependent SOX4 maintenance. Finally, TNFα increased SOX4 protein abundance in control PC3 and C4-2B cells, whereas this induction was not observed following ACAT1 depletion in either model (Fig. 3G).

Together, the unchanged SOX4 transcript abundance, reduced basal SOX4 protein abundance, MG132-mediated restoration, and loss of TNFα-induced accumulation indicate that ACAT1 is required for TNFα-responsive SOX4 protein maintenance and implicate a proteasome-sensitive post-transcriptional process.

ACAT1 and SOX4 exhibit an extranuclear pattern of spatial association in human prostate cancer tissue

Having established that ACAT1 was required for SOX4 protein maintenance in prostate cancer cell models, we next examined the spatial relationship between the two proteins in human prostate cancer tissue. Confocal immunofluorescence imaging of specimens from four independent cases revealed heterogeneous ACAT1 and SOX4 staining patterns, with Hoechst providing a nuclear reference. Although signal intensity and distribution varied among cases, merged images revealed focal overlap between ACAT1- and SOX4-positive regions (Fig. 4A). Three-channel line-intensity profiles showed coincident ACAT1 and SOX4 peaks at positions spatially separated from prominent Hoechst peaks, consistent with focal overlap outside

Hoechst-rich nuclear regions (Fig. 4B). Complementary ACAT1–SOX4 colocalization analysis using Coloc 2 yielded positive Pearson correlation coefficients of 0.70, 0.51, 0.67, and 0.67 in cases 1–4, respectively. Together, the line-profile and pixel-intensity analyses support a focal extranuclear pattern of spatial association between ACAT1 and a subset of SOX4 signals in human prostate cancer tissue.

ACAT1 loss induces lipid remodeling and extracellular lipid-dependent growth suppression

To define the metabolic consequences of ACAT1 depletion, we performed global metabolomic profiling of control and ACAT1-knockout PC3 cells. Principal component analysis revealed clear separation between the two groups, indicating distinct global metabolomic profiles (Fig. 5A, Supplementary Table S4). A heatmap of the differentially abundant metabolites further illustrated contrasting abundance patterns between control and ACAT1-knockout cells (Fig. 5B).

Analysis of the 20 canonical amino acids showed that ACAT1 loss significantly increased the abundance of arginine, histidine, isoleucine, leucine, lysine, methionine, phenylalanine, tryptophan, tyrosine, and valine while decreasing aspartate (Supplementary Figure 4A). Histidine and tyrosine were of particular interest because their corresponding metabolic gene sets showed negative enrichment in ERG-negative mCRPC relative to primary PCa and inverse correlations with progression-associated transcriptional programs in the primary-tumor scRNA-seq analysis (Fig. 1A, C). In contrast, alanine, asparagine, cysteine, glutamine, glutamate, glycine, proline, serine, and threonine were not significantly altered (Supplementary Figure 4B). Notably, cysteine, glutamate, and glycine—the three amino acid constituents of glutathione—were all unchanged, paralleling the absence of a significant correlation between the glutathione metabolism gene set and progression-associated programs in the scRNA-seq

analysis (Fig. 1C).

Metabolite set enrichment analysis using the differentially abundant metabolites identified phosphatidylethanolamine (PE) and phosphatidylcholine (PC) biosynthesis as the only pathways meeting the significance threshold (Fig. 5C). Choline, phosphoethanolamine (EAP), and ethanolamine, which mapped to these pathways, were significantly increased following ACAT1 loss (Fig. 5D). Given that the fatty acid metabolism gene set showed negative enrichment in ERG-negative mCRPC and an inverse association with progression-associated transcriptional programs (Fig. 1A, C), the prominence of phospholipid-associated changes prompted us to investigate lipid remodeling and its contribution to the growth-suppressive phenotype following ACAT1 loss.

Principal component analysis of the lipidomic profiles likewise distinguished control and ACAT1-knockout PC3 cells (Fig. 5E, Supplementary Table S5). A heatmap of the differentially abundant lipid species revealed extensive remodeling across multiple lipid classes, including increases in multiple ceramide species and alterations in polyunsaturated fatty acid (PUFA)-containing phospholipids (Fig. 5F). Lipid ontology analysis further highlighted long-chain and polyunsaturated lipid features, including lipids containing four double bonds and arachidonic acid (C20:4) (Supplementary Figure 5A). Several diacylglycerol (DG) and triacylglycerol (TG) species were also increased following ACAT1 loss (Supplementary Figure 5B), together with broad increases in endogenous ceramide species (Supplementary Figure 6A).

As an orthogonal, cell-based assessment of neutral lipid accumulation, we performed Oil Red O staining. Neutral lipid accumulation was significantly increased in ACAT1-knockout PC3 cells (Fig. 5G) and ACAT1-depleted C4-2B cells, whereas it was reduced following ACAT1 depletion in Du145 cells (Supplementary Figure 5C). We next asked whether the neutral lipid accumulation observed in PC3 cells was associated with impaired fatty acid β-oxidation.

ACAT1 loss did not significantly alter palmitate oxidation, whereas the carnitine palmitoyltransferase 1 (CPT1) inhibitor etomoxir markedly reduced oxidation, confirming assay responsiveness (Fig. 5H). Thus, the neutral lipid accumulation following ACAT1 loss was not accompanied by a detectable impairment in fatty acid β-oxidation under these conditions.

We then tested whether extracellular lipid availability contributed to the ACAT1-loss phenotype. Culture in delipidated serum markedly attenuated neutral lipid accumulation in ACAT1-knockout cells (Fig. 5I). This response was accompanied by restoration of AKT Ser473 phosphorylation within 24 h and subsequent attenuation of p27 accumulation at later time points (Fig. 5J), together with significant alleviation of the proliferation defect (Fig. 5K). Notably, reduced basal RelA/p65 phosphorylation and attenuated TNFα-induced RelA/p65 phosphorylation persisted under delipidated-serum conditions (Supplementary Figure 3D), in contrast to the restoration of AKT–p27 signaling and proliferation. These findings indicate that the NF-κB-associated defect was separable from the extracellular lipid-dependent growth response.

Finally, given the increase in multiple endogenous ceramide species following ACAT1 loss, we sought proof-of-principle that exogenous ceramide could reproduce selected features of the ACAT1-loss phenotype. To this end, we used cell-permeable C6-ceramide as a short-chain ceramide analog. C6-ceramide reduced cell viability in a dose-dependent manner in both PC3 and C4-2B cells (Supplementary Figure 6B). At the respective approximate IC_{50} concentrations of 3 μM for PC3 cells and 30 μM for C4-2B cells, C6-ceramide significantly suppressed cell proliferation in both models (Supplementary Figure 6C), accompanied by reduced AKT Ser473 phosphorylation and increased p27 protein abundance (Supplementary Figure 6D). Moreover, addition of C6-ceramide to ACAT1-knockout PC3 cells cultured in delipidated serum reversed

509 the recovery of AKT phosphorylation and reinstated p27 accumulation (Supplementary Figure
510 6E).
511 Together, extracellular lipid restriction alleviated neutral lipid accumulation and proliferative
512 suppression and reversed the ACAT1-loss-associated changes in AKT–p27 signaling, whereas
513 exogenous C6-ceramide reinstated the AKT–p27 response under lipid-depleted conditions and
514 suppressed proliferation in both models. These complementary findings support a role for
515 ACAT1 in buffering extracellular lipid-driven perturbations in lipid homeostasis, thereby
516 sustaining AKT signaling and cell proliferation.
517 **PPARγ contributes to lipid accumulation and growth suppression following ACAT1 loss**
518 Because SOX4 has previously been implicated in repressing PPARγ2 during adipogenic
519 commitment [43], we first examined whether SOX4 depletion elicited a PPARγ-associated
520 response in prostate cancer cells. SOX4 depletion reproduced selected effects of ACAT1 loss,
521 including reduced AKT Ser473 phosphorylation, increased p27 abundance, impaired
522 proliferation and gap closure, and increased neutral lipid accumulation (Supplementary Figure
523 7A–D). SOX4 depletion also increased PPARγ protein abundance in both PC3 and C4-2B cells
524 (Supplementary Figure 7E). These findings, together with the neutral lipid accumulation and
525 extracellular lipid-dependent growth suppression caused by ACAT1 loss, prompted us to
526 examine PPARγ abundance following ACAT1 depletion. PPARγ protein abundance was
527 increased in both ACAT1-depleted PC3 and C4-2B cells (Fig. 6A), identifying PPARγ
528 upregulation as a convergent response to SOX4 and ACAT1 depletion.
529 To test the functional contribution of PPARγ activity to the ACAT1-loss phenotype, we treated
530 control and ACAT1-knockout PC3 cells with the PPARγ antagonist GW9662. GW9662
531 reduced Oil Red O-positive neutral lipid accumulation in ACAT1-knockout cells (Fig. 6B) and
532 significantly alleviated their proliferation defect over 96 h (Fig. 6C). This proliferative recovery

was accompanied by increased AKT Ser473 phosphorylation and reduced p27 protein abundance relative to vehicle-treated ACAT1-knockout cells (Fig. 6D). However, GW9662 did not significantly restore gap closure (Fig. 6E).

Together, these findings support a functional contribution of PPARγ to neutral lipid accumulation, AKT–p27 signaling changes, and proliferative suppression following ACAT1 loss. The lack of significant restoration of gap closure suggests the involvement of additional ACAT1-dependent mechanisms that are not reversed by PPARγ antagonism. Integrating these results with the SOX4 and extracellular lipid-restriction experiments, we propose a model in which ACAT1 maintains SOX4 protein abundance and lipid homeostasis in ERG-negative prostate cancer cells, whereas its depletion elicits a PPARγ-associated lipid response that contributes to reduced AKT signaling and proliferative suppression (Fig. 7).

Discussion

Prostate cancer undergoes substantial metabolic reprogramming during progression [2–4], but whether this process differs between ERG-defined molecular subsets has remained unclear [5–7]. Our ERG-stratified analyses identified distinct progression-associated metabolic patterns and an EMT-like, AR-low tumor cell state characterized by high ACAT1 and SOX4 expression and reduced fatty acid metabolism gene-set activity. ACAT1 expression increased in the ERG-negative mCRPC-versus-primary comparison but not in the corresponding ERG-positive comparison. Functionally, ACAT1 depletion in PC3 and C4-2B cells suppressed proliferation, anchorage-independent growth, and gap closure and reduced AKT phosphorylation, consistent with the association between high ACAT1 expression and elevated AKT signature scores observed in the scRNA-seq analysis.

Global metabolomic profiling revealed broad metabolic changes following ACAT1 loss, including increased intracellular isoleucine and several other amino acids. Although ACAT1 is annotated within mitochondrial lipid catabolic pathways, its established physiological thiolase functions center on ketone-body utilization and terminal isoleucine catabolism, as illustrated by inherited ACAT1 deficiency [8,44,45]. Consistent with the latter function, ACAT1 depletion increased intracellular isoleucine abundance. The accompanying accumulation of valine, histidine, tyrosine, and several other amino acids suggests that the metabolic consequences of ACAT1 loss extend beyond its immediate substrates. Histidine and tyrosine were of particular interest because their corresponding metabolic gene sets were attenuated during ERG-negative metastatic progression and inversely associated with progression-related transcriptional programs. The mechanisms underlying these broader amino acid changes and their contribution to growth suppression remain unresolved.

Lipidomic profiling revealed extensive remodeling following ACAT1 loss, including increases

in multiple endogenous ceramide species and alterations in PUFA-containing phospholipids, DGs, and TGs. These changes affected both bioactive and storage lipid pools and were accompanied by neutral lipid accumulation. However, palmitate oxidation was not significantly altered, indicating that lipid accumulation was not explained by a detectable reduction in fatty acid β-oxidation under the conditions examined. The contribution of individual lipid species to the growth-suppressive phenotype remains unresolved.

The strongest functional connection between lipid remodeling and proliferative suppression was provided by the delipidated-serum experiments. Restriction of extracellular lipids attenuated neutral lipid accumulation, restored AKT phosphorylation, reduced p27 accumulation, and alleviated the proliferation defect caused by ACAT1 loss. Extracellular lipid availability was therefore a major determinant of this phenotype. In prostate cancer, extracellular fatty acids contribute to tumor lipid synthesis, while periprostatic adipose tissue can supply lipids to adjacent tumor cells [46,47]. Although extracellular lipids generally support prostate cancer growth, their effects also depend on how acquired lipids are processed, stored, and remodeled [3,4,46,48]. Complementing these findings, C6-ceramide suppressed proliferation, reduced AKT phosphorylation, increased p27 abundance, and reversed the signaling recovery produced by delipidated serum. This provided proof of principle that an externally supplied lipid can modify the AKT–p27–proliferation response. Because C6-ceramide is a cell-permeable short-chain analog distinct from the endogenous long-chain ceramide species increased following ACAT1 loss, these experiments do not identify a specific endogenous ceramide as the mediator of the phenotype. Together, these findings suggest that ACAT1 enables a subset of ERG-negative prostate cancer cells to maintain lipid homeostasis and proliferative signaling in a lipid-replete environment, whereas its loss converts extracellular lipid exposure into a maladaptive, growth-suppressive response.

PPARγ provided an additional functional link between ACAT1 loss, lipid accumulation, and proliferative suppression. ACAT1 depletion increased PPARγ protein abundance in both PC3 and C4-2B cells, and pharmacological PPARγ antagonism with GW9662 reduced neutral lipid accumulation in ACAT1-knockout PC3 cells. GW9662 also partially restored proliferation and shifted AKT–p27 signaling toward the control state, supporting a contribution of the PPARγ-associated lipid response to the growth-suppressive phenotype. However, GW9662 did not significantly restore gap closure, indicating that PPARγ contributes selectively to the lipid and proliferative consequences of ACAT1 loss rather than accounting for all ACAT1-dependent phenotypes.

A second central finding of this study is that ACAT1 maintains a proteasome-sensitive SOX4 protein pool. ACAT1 depletion reduced SOX4 protein without decreasing its mRNA, and proteasome inhibition brought SOX4 abundance to similar levels in control and depleted cells in both PC3 and C4-2B models. ACAT1 loss also prevented TNFα-induced SOX4 accumulation in both models. Chloroquine responses differed between models, suggesting a cell context-dependent contribution of lysosome-sensitive regulation. Previous work showed that inflammatory cytokines stabilize SOXC proteins through a post-transcriptional, proteasome-sensitive process [37], while the degradation-sensitive C-terminal region of SOX4 can be protected by the adaptor protein syntenin [49]. Together, these findings identify ACAT1 as a determinant of basal and TNFα-responsive SOX4 protein abundance. Tissue imaging revealed focal extranuclear association between ACAT1 and a subset of SOX4 signals in human prostate cancer specimens, providing spatial context for ACAT1-dependent SOX4 regulation.

SOX4 depletion reproduced selected signaling, proliferative, migratory, and lipid-associated phenotypes observed following ACAT1 loss and was accompanied by increased PPARγ abundance. These findings support functional convergence between ACAT1 loss and SOX4

depletion and suggest that ACAT1-dependent SOX4 maintenance may contribute to the PPARγ-associated lipid response. However, the molecular mechanism by which ACAT1 maintains SOX4 protein abundance and whether the metabolic consequences of ACAT1 loss are mediated through a linear ACAT1–SOX4–PPARγ axis remain unresolved. Future studies should define this mechanism and use mechanism-guided approaches to restore SOX4 protein abundance in ACAT1-knockout cells.

Although identified in prostate cancer cells, ACAT1-dependent maintenance of SOX4 protein may not be restricted to this disease context. ACAT1 exerts metabolic and post-translational regulatory functions in multiple tumor types [50–53], while SOX4 broadly contributes to tumor progression and cell-state plasticity [54–57]. Examining whether ACAT1 similarly regulates a proteasome-sensitive SOX4 pool in other malignancies and inflammatory contexts will help determine the broader relevance of this regulatory relationship.

The weaker response to ACAT1 depletion in Du145 cells further indicates that ACAT1 dependency is cell context-dependent. Although Du145 cells do not harbor the canonical TMPRSS2–ERG fusion, ERG mRNA was detectable under our experimental conditions, consistent with a previous report showing low ERG protein expression in this cell line [58]. Accordingly, whereas the clinical transcriptomic analyses were stratified by TMPRSS2–ERG fusion status, the cell-line experiments distinguished ERG-undetectable PC3 and C4-2B cells from ERG-detectable Du145 cells. This distinction may be biologically relevant because the principal consequence of the TMPRSS2–ERG rearrangement is aberrant ERG expression under androgen-responsive TMPRSS2 regulatory elements rather than acquisition of a TMPRSS2-derived protein domain. ERG expression itself may therefore influence cellular behavior irrespective of the mechanism responsible for its expression. ERG has also been reported to interact with SOX4 and cooperate with it in EMT-associated transcriptional

programs [59]. However, because ERG abundance in Du145 cells is low and the cell lines differ in multiple molecular features, isogenic ERG gain- and loss-of-function models will be required to determine whether ERG expression directly modifies ACAT1 dependency.

A limitation of this study is that the functional analyses were conducted primarily in vitro. However, previous clinical and in vivo studies support the disease relevance of ACAT1 in prostate cancer. Proteomic and tissue-based analyses identified increased ACAT1 abundance in high-grade, metastatic, and castration-resistant prostate cancer [9–11], and ACAT1 protein expression independently predicted biochemical recurrence, with prognostic separation observed specifically in ERG-negative disease [10]. Functional studies have further implicated ACAT1 in prostate cancer cell proliferation, invasion, migration, xenograft growth, pollutant-induced aggressiveness, and survival during enzalutamide exposure [12–15]. More recently, pharmacological ACAT1 blockade increased lipid accumulation and lipid uptake in prostate cancer cells, reduced the viability of PDX-derived organoids, and suppressed tumor growth in multiple prostate cancer PDX models [60]. These independent observations support the in vivo and clinical relevance of ACAT1 and corroborate the association between ACAT1 inhibition and altered lipid homeostasis observed in the present study. Nevertheless, ACAT1-dependent SOX4 protein maintenance and the PPARγ-associated lipid response identified here require direct validation in vivo.

Conclusions

Multi-cohort transcriptomic analyses revealed reduced fatty acid metabolism gene-set activity and elevated ACAT1 expression in ERG-negative mCRPC and the progression-associated Cluster 5 state, with fatty acid metabolism scores inversely correlated with prostate cancer progression signature scores across tumor cell clusters. ACAT1 supports proliferative and aggressive phenotypes in ERG-negative prostate cancer cells, maintains basal and TNFα-induced SOX4 protein abundance, and restrains PPARγ-associated lipid remodeling. Limiting extracellular lipid availability attenuated neutral lipid accumulation, restored AKT–p27 signaling, and alleviated proliferative suppression following ACAT1 loss, identifying extracellular lipids as a major determinant of this phenotype. PPARγ antagonism similarly reduced lipid accumulation and partially restored AKT–p27 signaling and proliferation, supporting a functional contribution of the PPARγ-associated response. SOX4 depletion reproduced selected signaling, lipid, and growth phenotypes of ACAT1 loss, while human tissue imaging revealed focal extranuclear spatial association between ACAT1 and SOX4. Collectively, these findings identify ACAT1 as a regulator of SOX4 protein maintenance and lipid homeostasis that supports the growth of ERG-negative prostate cancer cells.

List of abbreviations

ACAT1: Acetyl-CoA acetyltransferase 1

AKT: Protein kinase B

AR: Androgen receptor

AUC: Area under the curve

CE–TOFMS: Capillary electrophoresis–time-of-flight mass spectrometry

CPT1: Carnitine palmitoyltransferase 1

CQ: Chloroquine

DG: Diacylglycerol

EAP: Phosphoethanolamine

EMT: Epithelial–mesenchymal transition

ERG: ETS-related gene

FBS: Fetal bovine serum

GSEA: Gene set enrichment analysis

IC_{50}: Half-maximal inhibitory concentration

KEGG: Kyoto Encyclopedia of Genes and Genomes

LC–MS/MS: Liquid chromatography–tandem mass spectrometry

LION: Lipid Ontology

mCRPC: Metastatic castration-resistant prostate cancer

MMP: Matrix metalloproteinase

MSEA: Metabolite set enrichment analysis

NF-κB: Nuclear factor kappa B

PC: Phosphatidylcholine

PCa: Prostate cancer

PCA: Principal component analysis

PDX: Patient-derived xenograft

PE: Phosphatidylethanolamine

PPARγ: Peroxisome proliferator-activated receptor gamma

PUFA: Polyunsaturated fatty acid

SA-β-gal: Senescence-associated β-galactosidase

scRNA-seq: Single-cell RNA sequencing

SOX4: SRY-box transcription factor 4

ssGSEA: Single-sample gene set enrichment analysis

TCGA-PRAD: The Cancer Genome Atlas Prostate Adenocarcinoma

TG: Triacylglycerol

TNFα: Tumor necrosis factor alpha

UMAP: Uniform Manifold Approximation and Projection

Declarations

Ethics approval and consent to participate

This study was reviewed by the Institutional Review Board of the Gwangju Institute of Science and Technology (approval no. 20240620-BR-EX-015).

Consent for publication

Not applicable.

Availability of data and materials

The publicly available datasets analyzed in this study are available from the Gene Expression Omnibus under accession numbers GSE32269 and GSE176031 and from The Cancer Genome Atlas Prostate Adenocarcinoma (TCGA-PRAD) cohort. Data generated during this study are included in the article and its additional files.

Competing interests

The authors declare that they have no competing interests.

Funding

This work was supported by grants from the National Research Foundation of Korea (RS-2023-00252326 and RS-2026-25603010) and, in part, by a grant from the Korea Health Technology R&D Project through the Korea Health Industry Development Institute (KHIDI), funded by the Ministry of Health & Welfare, Republic of Korea (RS-2026-25537126). This study was also supported by GIST Research Funds (GRI IIBR grant and the 2026 Future-Leading Specialized Research Project).

Authors' contributions

SHP conceived the study, designed and performed the experiments, analyzed and interpreted the data, conducted the bioinformatic analyses, prepared the figures, and wrote the original manuscript. SHS contributed to the metabolomic analysis. SWS performed the lipidomic analysis and contributed to lipidomic data interpretation. SGY, JYH, and DYC provided human prostate cancer tissue specimens and contributed clinical and pathological expertise. KWK supervised metabolomic data interpretation. TYK supervised the lipidomic analysis and contributed to data interpretation. SKC conceived and supervised the study, administered the project, acquired funding, and critically revised the manuscript. All authors reviewed and approved the final manuscript.

741 **Acknowledgements**

742 The authors thank Ms. Rosalind H. Lee (FGL, Gwangju Institute of Science and Technology
743 [GIST]) for providing guidance on the bioinformatic analyses. The authors also acknowledge
744 the use of the confocal laser scanning microscope (FV3000RS, Olympus, BI03) through the
745 GAIA research equipment platform at GIST.

References

1. Rebello RJ, Oing C, Knudsen KE, Loeb S, Johnson DC, Reiter RE, et al. Prostate cancer. Nat Rev Dis Primers. 2021;7:9. https://doi.org/10.1038/s41572-020-00243-0.

2. Pujana-Vaquerizo M, Bozal-Basterra L, Carracedo A. Metabolic adaptations in prostate cancer. Br J Cancer. 2024;131:1250–1262. https://doi.org/10.1038/s41416-024-02762-z.

3. Giafaglione JM, Crowell PD, Delcourt AML, Hashimoto T, Ha SM, Atmakuri A, et al. Prostate lineage-specific metabolism governs luminal differentiation and response to antiandrogen treatment. Nat Cell Biol. 2023;25:1821–1832. https://doi.org/10.1038/s41556-023-01274-x.

4. Scheinberg T, Mak B, Butler L, Selth L, Horvath LG. Targeting lipid metabolism in metastatic prostate cancer. Ther Adv Med Oncol. 2023;15:17588359231152839. https://doi.org/10.1177/17588359231152839.

5. Tomlins SA, Rhodes DR, Perner S, Dhanasekaran SM, Mehra R, Sun XW, et al. Recurrent fusion of TMPRSS2 and ETS transcription factor genes in prostate cancer. Science. 2005;310:644–648. https://doi.org/10.1126/science.1117679.

6. Cancer Genome Atlas Research Network. The molecular taxonomy of primary prostate cancer. Cell. 2015;163:1011–1025. https://doi.org/10.1016/j.cell.2015.10.025.

7. Song H, Weinstein HNW, Allegakoen P, Wadsworth MH II, Xie J, Yang H, et al. Single-cell analysis of human primary prostate cancer reveals the heterogeneity of tumor-associated epithelial cell states. Nat Commun. 2022;13:141. https://doi.org/10.1038/s41467-021-27322-4.

8. Goudarzi A. The recent insights into the function of ACAT1: a possible anti-cancer therapeutic target. Life Sci. 2019;232:116592. https://doi.org/10.1016/j.lfs.2019.116592.

9. Saraon P, Cretu D, Musrap N, Karagiannis GS, Batruch I, Drabovich AP, et al. Quantitative proteomics reveals that enzymes of the ketogenic pathway are associated with prostate cancer

770 progression. Mol Cell Proteomics. 2013;12:1589–1601.
771 https://doi.org/10.1074/mcp.M112.023887.
772 10. Saraon P, Trudel D, Kron K, Dmitromanolakis A, Trachtenberg J, Bapat B, et al. Evaluation
773 and prognostic significance of ACAT1 as a marker of prostate cancer progression. Prostate.
774 2014;74:372–380. https://doi.org/10.1002/pros.22758.
775 11. Labanca E, Bizzotto J, Sanchis P, Anselmino N, Yang J, Shepherd PDA, et al. Prostate
776 cancer castrate-resistant progression usage of non-canonical androgen receptor signaling and
777 ketone-body fuel. Oncogene. 2021;40:6284–6298. https://doi.org/10.1038/s41388-021-02008-
778 9.
779 12. Guan J, Jiang X, Gai J, Sun X, Zhao J, Li J, et al. Sirtuin 5 regulates the proliferation,
780 invasion and migration of prostate cancer cells through acetyl-CoA acetyltransferase 1. J Cell
781 Mol Med. 2020;24:14039–14049. https://doi.org/10.1111/jcmm.16016.
782 13. Guan J, Jiang X, Guo Y, Zhao W, Li J, Li Y, et al. Autophagy inhibition and reactive oxygen
783 species elimination by acetyl-CoA acetyltransferase 1 through fused in sarcoma protein to
784 promote prostate cancer. BMC Cancer. 2022;22:1313. https://doi.org/10.1186/s12885-022-
785 10426-5.
786 14. Buñay J, Kossai M, Damon-Soubeyrant C, De Haze A, Saru JP, Trousson A, et al. Persistent
787 organic pollutants promote aggressiveness in prostate cancer. Oncogene. 2023;42:2854–2867.
788 https://doi.org/10.1038/s41388-023-02788-2.
789 15. Kohrt SE, Awadallah WN, Phillips RA III, Case TC, Jin R, Nanda JS, et al. Identification
790 of genes required for enzalutamide resistance in castration-resistant prostate cancer cells in
791 vitro. Mol Cancer Ther. 2021;20:398–409. https://doi.org/10.1158/1535-7163.MCT-20-0244.
792 16. Hosios AM, Li Z, Lien EC, Vander Heiden MG. Preparation of lipid-stripped serum for the
793 study of lipid metabolism in cell culture. Bio Protoc. 2018;8(11):e2876.

https://doi.org/10.21769/BioProtoc.2876.

17. Folch J, Lees M, Sloane Stanley GH. A simple method for the isolation and purification of total lipides from animal tissues. J Biol Chem. 1957;226:497–509. https://doi.org/10.1016/S0021-9258(18)64849-5.

18. Bishop LM, Fiehn O. Comprehensive lipidomic profiling by plasma separation cards. Anal Bioanal Chem. 2023;415:193–201. https://doi.org/10.1007/s00216-022-04399-4.

19. Koelmel JP, Li X, Stow SM, Sartain MJ, Murali A, Kemperman R, et al. Lipid Annotator: towards accurate annotation in non-targeted liquid chromatography high-resolution tandem mass spectrometry lipidomics using a rapid and user-friendly software. Metabolites. 2020;10:101. https://doi.org/10.3390/metabo10030101.

20. Pang Z, Lu Y, Zhou G, Hui F, Xu L, Viau C, et al. MetaboAnalyst 6.0: towards a unified platform for metabolomics data processing, analysis and interpretation. Nucleic Acids Res. 2024;52(W1):W398–W406. https://doi.org/10.1093/nar/gkae253.

21. Molenaar MR, Jeucken A, Wassenaar TA, van de Lest CHA, Brouwers JFHM, Helms JB. LION/web: a web-based ontology enrichment tool for lipidomic data analysis. GigaScience. 2019;8(6):giz061. https://doi.org/10.1093/gigascience/giz061.

22. R Core Team. R: A language and environment for statistical computing. Vienna, Austria: R Foundation for Statistical Computing; 2024. Available from: https://www.R-project.org/.

23. Cai C, Wang H, He HH, Chen S, He L, Ma F, et al. ERG induces androgen receptor-mediated regulation of SOX9 in prostate cancer. J Clin Invest. 2013;123:1109–1122. https://doi.org/10.1172/JCI66666.

24. Wu T, Hu E, Xu S, Chen M, Guo P, Dai Z, et al. clusterProfiler 4.0: a universal enrichment tool for interpreting omics data. Innovation (Camb). 2021;2(3):100141. https://doi.org/10.1016/j.xinn.2021.100141.

818 25. Hao Y, Stuart T, Kowalski MH, Choudhary S, Hoffman P, Hartman A, et al. Dictionary
819 learning for integrative, multimodal and scalable single-cell analysis. Nat Biotechnol.
820 2024;42:293–304. https://doi.org/10.1038/s41587-023-01767-y.
821 26. Hänzelmann S, Castelo R, Guinney J. GSVA: gene set variation analysis for microarray
822 and RNA-seq data. BMC Bioinformatics. 2013;14:7. https://doi.org/10.1186/1471-2105-14-7.
823 27. Wang G, Wang J, Sadar MD. Crosstalk between the androgen receptor and beta-catenin in
824 castrate-resistant prostate cancer. Cancer Res. 2008;68:9918–9927.
825 https://doi.org/10.1158/0008-5472.CAN-08-1718.
826 28. Ouyang X, Jessen WJ, Al-Ahmadie H, Serio AM, Lin Y, Shih WJ, et al. Activator protein-
827 1 transcription factors are associated with progression and recurrence of prostate cancer. Cancer
828 Res. 2008;68:2132–2144. https://doi.org/10.1158/0008-5472.CAN-07-6055.
829 29. Majumder PK, Febbo PG, Bikoff R, Berger R, Xue Q, McMahon LM, et al. mTOR
830 inhibition reverses Akt-dependent prostate intraepithelial neoplasia through regulation of
831 apoptotic and HIF-1-dependent pathways. Nat Med. 2004;10:594–601.
832 https://doi.org/10.1038/nm1052.
833 30. Liberzon A, Birger C, Thorvaldsdóttir H, Ghandi M, Mesirov JP, Tamayo P. The Molecular
834 Signatures Database (MSigDB) hallmark gene set collection. Cell Syst. 2015;1:417–425.
835 https://doi.org/10.1016/j.cels.2015.12.004.
836 31. Tang Z, Kang B, Li C, Chen T, Zhang Z. GEPIA2: an enhanced web server for large-scale
837 expression profiling and interactive analysis. Nucleic Acids Res. 2019;47(W1):W556–W560.
838 https://doi.org/10.1093/nar/gkz430.
839 32. Hashemi M, Taheriazam A, Daneii P, Hassanpour A, Kakavand A, Rezaei S, et al. Targeting
840 PI3K/Akt signaling in prostate cancer therapy. J Cell Commun Signal. 2023;17:423–443.
841 https://doi.org/10.1007/s12079-022-00702-1.

842 33. Kreisberg JI, Malik SN, Prihoda TJ, Bedolla RG, Troyer DA, Kreisberg S, et al.
843 Phosphorylation of Akt (Ser473) is an excellent predictor of poor clinical outcome in prostate
844 cancer. Cancer Res. 2004;64:5232–5236. https://doi.org/10.1158/0008-5472.CAN-04-0272.
845 34. Fang Z, Zhang T, Dizeyi N, Chen S, Wang H, Swanson KD, et al. Androgen receptor
846 enhances p27 degradation in prostate cancer cells through rapid and selective TORC2
847 activation. J Biol Chem. 2012;287:2090–2098. https://doi.org/10.1074/jbc.M111.323303.
848 35. Revandkar A, Perciato ML, Toso A, Alajati A, Chen J, Gerber H, et al. Inhibition of Notch
849 pathway arrests PTEN-deficient advanced prostate cancer by triggering p27-driven cellular
850 senescence. Nat Commun. 2016;7:13719. https://doi.org/10.1038/ncomms13719.
851 36. Buss H, Dörrie A, Schmitz ML, Hoffmann E, Resch K, Kracht M. Constitutive and
852 interleukin-1-inducible phosphorylation of p65 NF-κB at serine 536 is mediated by multiple
853 protein kinases including IκB kinase (IKK)-α, IKKβ, IKKε, TRAF family member-associated
854 (TANK)-binding kinase 1 (TBK1), and an unknown kinase and couples p65 to TATA-binding
855 protein-associated factor II31-mediated interleukin-8 transcription. J Biol Chem.
856 2004;279:55633–55643. https://doi.org/10.1074/jbc.M409825200.
857 37. Bhattaram P, Muschler G, Wixler V, Lefebvre V. Inflammatory cytokines stabilize SOXC
858 transcription factors to mediate the transformation of fibroblast-like synoviocytes in arthritic
859 disease. Arthritis Rheumatol. 2018;70:371–382. https://doi.org/10.1002/art.40386.
860 38. Jones K, Ramirez-Perez S, Niu S, Gangishetti U, Drissi H, Bhattaram P. SOX4 and RELA
861 function as transcriptional partners to regulate the expression of TNF-responsive genes in
862 fibroblast-like synoviocytes. Front Immunol. 2022;13:789349.
863 https://doi.org/10.3389/fimmu.2022.789349.
864 39. Sasaki CY, Barberi TJ, Ghosh P, Longo DL. Phosphorylation of RelA/p65 on serine 536
865 defines an IκBα-independent NF-κB pathway. J Biol Chem. 2005;280:34538–34547.

https://doi.org/10.1074/jbc.M504943200.

40. Adli M, Baldwin AS. IKK-i/IKKε controls constitutive, cancer cell-associated NF-κB activity via regulation of Ser-536 p65/RelA phosphorylation. J Biol Chem. 2006;281:26976–26984. https://doi.org/10.1074/jbc.M603133200.

41. Huang S, Pettaway CA, Uehara H, Bucana CD, Fidler IJ. Blockade of NF-κB activity in human prostate cancer cells is associated with suppression of angiogenesis, invasion, and metastasis. Oncogene. 2001;20:4188–4197. https://doi.org/10.1038/sj.onc.1204535.

42. Nalla AK, Gorantla B, Gondi CS, Lakka SS, Rao JS. Targeting MMP-9, uPAR, and cathepsin B inhibits invasion, migration and activates apoptosis in prostate cancer cells. Cancer Gene Ther. 2010;17:599–613. https://doi.org/10.1038/cgt.2010.16.

43. He T, Wang S, Li S, Shen H, Hou L, Liu Y, et al. Suppression of preadipocyte determination by SOX4 limits white adipocyte hyperplasia in obesity. iScience. 2023;26:106289. https://doi.org/10.1016/j.isci.2023.106289.

44. Li Z, Liu S, Jin W, Xiao L, Kester O, Bullen N, et al. Isoleucine and valine promote prostate cancer progression via propionyl-CoA-mediated cholesterol metabolism. Nat Metab. 2026;8:1772–1790. https://doi.org/10.1038/s42255-026-01583-z.

45. Grünert SC, Sass JO. 2-Methylacetoacetyl-coenzyme A thiolase (beta-ketothiolase) deficiency: one disease—two pathways. Orphanet J Rare Dis. 2020;15:106. https://doi.org/10.1186/s13023-020-01357-0.

46. Balaban S, Nassar ZD, Zhang AY, Hosseini-Beheshti E, Centenera MM, Schreuder M, et al. Extracellular fatty acids are the major contributor to lipid synthesis in prostate cancer. Mol Cancer Res. 2019;17:949–962. https://doi.org/10.1158/1541-7786.MCR-18-0347.

47. Altuna-Coy A, Ruiz-Plazas X, Sánchez-Martin S, Ascaso-Til H, Prados-Saavedra M, Alves-Santiago M, et al. The lipidomic profile of the tumoral periprostatic adipose tissue

reveals alterations in tumor cell's metabolic crosstalk. BMC Med. 2022;20:255. https://doi.org/10.1186/s12916-022-02457-3.

48. Butler LM, Mah CY, Machiels J, Vincent AD, Irani S, Mutuku SM, et al. Lipidomic profiling of clinical prostate cancer reveals targetable alterations in membrane lipid composition. Cancer Res. 2021;81:4981–4993. https://doi.org/10.1158/0008-5472.CAN-20-3863.

49. Beekman JM, Vervoort SJ, Dekkers F, van Vessem ME, Vendelbosch S, Brugulat-Panes A, et al. Syntenin-mediated regulation of SOX4 proteasomal degradation modulates transcriptional output. Oncogene. 2012;31:2668–2679. https://doi.org/10.1038/onc.2011.445.

50. Fan J, Shan C, Kang HB, Elf S, Xie J, Tucker M, et al. Tyr phosphorylation of PDP1 toggles recruitment between ACAT1 and SIRT3 to regulate the pyruvate dehydrogenase complex. Mol Cell. 2014;53:534–548. https://doi.org/10.1016/j.molcel.2013.12.026.

51. Fan J, Lin R, Xia S, Chen D, Elf SE, Liu S, et al. Tetrameric acetyl-CoA acetyltransferase 1 is important for tumor growth. Mol Cell. 2016;64:859–874. https://doi.org/10.1016/j.molcel.2016.10.014.

52. Zhu Y, Gu L, Lin X, Liu C, Lu B, Cui K, et al. Dynamic regulation of ME1 phosphorylation and acetylation affects lipid metabolism and colorectal tumorigenesis. Mol Cell. 2020;77:138–149.e5. https://doi.org/10.1016/j.molcel.2019.10.015.

53. Gu L, Zhu Y, Lin X, Tan X, Lu B, Li Y. Stabilization of FASN by ACAT1-mediated GNPAT acetylation promotes lipid metabolism and hepatocarcinogenesis. Oncogene. 2020;39:2437–2449. https://doi.org/10.1038/s41388-020-1156-0.

54. Liu P, Ramachandran S, Seyed MA, Scharer CD, Laycock N, Dalton WB, et al. Sex-determining region Y box 4 is a transforming oncogene in human prostate cancer cells. Cancer Res. 2006;66:4011–4019. https://doi.org/10.1158/0008-5472.CAN-05-3055.

914 55. Wang L, Zhang J, Yang X, Chang YW, Qi M, Zhou Z, et al. SOX4 is associated with poor
915 prognosis in prostate cancer and promotes epithelial–mesenchymal transition in vitro. Prostate
916 Cancer Prostatic Dis. 2013;16:301–307. https://doi.org/10.1038/pcan.2013.25.
917 56. Bilir B, Osunkoya AO, Wiles WG IV, Sannigrahi S, Lefebvre V, Metzger D, et al. SOX4 is
918 essential for prostate tumorigenesis initiated by PTEN ablation. Cancer Res. 2016;76:1112–
919 1121. https://doi.org/10.1158/0008-5472.CAN-15-1868.
920 57. Moreno CS. SOX4: The unappreciated oncogene. Semin Cancer Biol. 2020;67:57–64.
921 https://doi.org/10.1016/j.semcancer.2019.08.027.
922 58. Smith R, Liu M, Liby T, Bayani N, Bucher E, Chiotti K, et al. Enzalutamide response in a
923 panel of prostate cancer cell lines reveals a role for glucocorticoid receptor in enzalutamide
924 resistant disease. Sci Rep. 2020;10:21750. https://doi.org/10.1038/s41598-020-78798-x.
925 59. Wang L, Li Y, Yang X, Yuan H, Li X, Qi M, et al. ERG–SOX4 interaction promotes
926 epithelial–mesenchymal transition in prostate cancer cells. Prostate. 2014;74:647–658.
927 https://doi.org/10.1002/pros.22783.
928 60. Sanchis P, Sabater AA, Dong J, Shepherd P, Anselmino N, Corn PG, et al. Exploiting ketone
929 body metabolism as a therapeutic vulnerability in prostate cancer. Cancer Res. 2026;86(7
930 Suppl):Abstract 4740. https://doi.org/10.1158/1538-7445.AM2026-4740.

Figure Legends

Fig. 1. Integrated transcriptomic analyses identify ACAT1 in a progression-associated, metabolism-low cell state in ERG-negative prostate cancer.

(A) Gene set enrichment analysis (GSEA) comparing metastatic castration-resistant prostate cancer (mCRPC) with primary prostate cancer (PCa) in GSE32269, stratified by ERG status.

(B) UMAP of ERG-negative tumor cells in GSE176031 (left) and a dot plot of KLF2, SOX4, VIM, CDH1, and AR expression across clusters (right).

(C) Heatmap of single-sample gene set enrichment analysis (ssGSEA) scores for the indicated transcriptional signatures and metabolic gene sets (left). Per-cell scores were summarized as cluster medians and standardized as Z-scores for each gene set. Scatter plots show relationships between the progression signature and the indicated signature scores (right). Each dot represents one cluster, Pearson correlation coefficients are indicated. Cluster 5 is highlighted in red.

(D) Schematic of candidate selection integrating GSE176031, GSE32269, and TCGA-PRAD.

(E) Violin plots of ACAT1 expression across ERG-negative tumor cell clusters in GSE176031.

(F) Violin plots of ACAT1 expression across ERG-defined primary PCa and mCRPC groups in GSE32269.

(G) Kaplan–Meier overall survival analysis in TCGA-PRAD, stratified by median ACAT1 expression into high (red) and low (blue) groups. The log-rank P value is indicated.

(H) ACAT1 mRNA expression [log2(normalized count + 1)] versus Cluster 5 signature ssGSEA scores in TCGA-PRAD. Each dot represents one tumor, the Spearman correlation coefficient is indicated.

Fig. 2. ACAT1 is required to maintain proliferative and aggressive phenotypes in ERG-negative prostate cancer cells.

(A) Proliferation of the indicated control and ACAT1-depleted cell lines over 96 h. Cell numbers at the indicated time points are presented.

(B) Anchorage-independent growth of the indicated control and ACAT1-depleted ERG-negative prostate cancer cell lines in soft agar. Colonies exceeding 50 μm in diameter were counted. Representative images are shown at ×40 magnification. Scale bars, 50 μm.

(C) Wound-healing assays of the indicated control and ACAT1-depleted ERG-negative prostate cancer cell lines over 24 h. Gap closure was calculated as the difference between the gap areas at 0 and 24 h. Representative images are shown at ×4 magnification. Scale bars, 500 μm.

(D) Immunoblot analysis of ACAT1, phosphorylated AKT at Ser473, total AKT, and p27.

(E) Senescence-associated β-galactosidase (SA-β-gal) staining of the indicated control and ACAT1-depleted cell lines. Representative images are shown at ×40 magnification. Scale bars, 50 μm.

(F) Immunoblot analysis of the senescence-associated marker lamin B1 in the indicated control and ACAT1-depleted cell lines.

Fig. 3. ACAT1 is required for TNFα-induced SOX4 accumulation.

(A) Schematic illustrating TNFα-induced RelA phosphorylation at Ser536 and proteasome-sensitive SOX4 protein stabilization. The solid arrow denotes an established signaling pathway, whereas the dashed arrow indicates reported SOX4 stabilization through an unresolved molecular mechanism.

(B) Immunoblot analysis of basal RelA/p65 phosphorylation at Ser536 and total RelA/p65 protein abundance in control and ACAT1-knockout PC3 cells.

(C) Immunoblot analysis of RelA/p65 phosphorylation at Ser536 and total RelA/p65 in control and ACAT1-knockdown C4-2B cells following treatment with TNFα (10 ng/mL) for 30 min.

(D) SOX4 mRNA expression in the indicated control and ACAT1-depleted PC3 and C4-2B cells.

(E) Immunoblot analysis of SOX4 protein abundance in the indicated control and ACAT1-depleted PC3 and C4-2B cells.

(F) Immunoblot analysis of ACAT1 and SOX4 in control and ACAT1-depleted PC3 and C4-2B cells treated with vehicle, MG132 (10 μM), chloroquine (CQ, 10 μM), or their combination for 4 h.

(G) Immunoblot analysis of the indicated proteins in control and ACAT1-depleted PC3 and C4-2B cells following treatment with TNFα (10 ng/mL) for 4 h.

Fig. 4. ACAT1 and SOX4 exhibit an extranuclear pattern of spatial association in human prostate cancer tissue.

(A) Representative confocal immunofluorescence images of four independent human prostate cancer cases stained for ACAT1 (green), SOX4 (red), and nuclei (Hoechst, blue). Single-channel and merged images show the distribution of each signal and focal overlap between ACAT1- and SOX4-positive regions. White lines indicate the positions used for the line-intensity profiles in (B). Scale bars, 100 μm.

(B) Three-channel line-intensity profiles from the corresponding tissue images in (A). Fluorescence intensities of ACAT1 (green), SOX4 (red), and Hoechst (blue) were measured along identical line selections and plotted against distance. Coloc 2-derived Pearson correlation coefficients for ACAT1 and SOX4 are indicated for each case.

Fig. 5. ACAT1 loss induces lipid remodeling and extracellular lipid-dependent growth suppression.

(A) Principal component analysis (PCA) of global metabolomic profiles from control and ACAT1-knockout (sgACAT1) PC3 cells. Cells were incubated in fresh medium for 4 h before metabolite extraction.

(B) Heatmap showing the relative abundance of differentially abundant metabolites in control and ACAT1-knockout PC3 cells.

(C) Metabolite set enrichment analysis (MSEA) of the differentially abundant metabolites identified in control and ACAT1-knockout PC3 cells.

(D) Relative abundance of choline, phosphoethanolamine (EAP), and ethanolamine, which mapped to phosphatidylcholine (PC) and phosphatidylethanolamine (PE) biosynthesis pathways, in control and ACAT1-knockout PC3 cells.

(E) PCA of global lipidomic profiles from control and ACAT1-knockout PC3 cells. Cells were incubated in fresh medium for 4 h before lipid extraction.

(F) Heatmap showing the relative abundance of differentially abundant lipid species in control and ACAT1-knockout PC3 cells.

(G) Oil Red O staining of control and ACAT1-knockout PC3 cells. Representative images are shown at ×40 magnification. Scale bars, 50 μm.

(H) Fatty acid β-oxidation in control and ACAT1-knockout PC3 cells measured using [9,10-^{3}H(N)]palmitic acid. Etomoxir (10 μM) was used as an inhibitor of carnitine palmitoyltransferase 1 (CPT1)-dependent fatty acid oxidation.

(I) Oil Red O staining of control and ACAT1-knockout PC3 cells cultured in normal or delipidated serum for 24 h. Representative images are shown at ×40 magnification. Scale bars, 50 μm.

(J) Immunoblot analysis of phosphorylated AKT at Ser473, total AKT, and p27 in control and ACAT1-knockout PC3 cells under normal-serum conditions and in ACAT1-knockout cells cultured in delipidated serum for 24 or 48 h.

(K) Proliferation of control and ACAT1-knockout PC3 cells cultured in normal or delipidated serum over 96 h. Cell numbers at the indicated time points are presented.

Fig. 6. PPARγ contributes to lipid accumulation and growth suppression following ACAT1 loss.

(A) Immunoblot analysis of SOX4 and PPARγ protein abundance in control and ACAT1-depleted PC3 and C4-2B cells.

(B) Oil Red O staining of control and ACAT1-knockout PC3 cells treated with vehicle or the PPARγ antagonist GW9662 (20 nM). Cells were treated with GW9662 for 48 h before Oil Red O staining. Representative images are shown at ×40 magnification. Scale bars, 50 μm.

(C) Proliferation of control and ACAT1-knockout PC3 cells treated with vehicle or GW9662 (20 nM) over 96 h. Cell numbers at the indicated time points are presented.

(D) Immunoblot analysis of phosphorylated AKT at Ser473, total AKT, and p27 in control and ACAT1-knockout PC3 cells treated with vehicle or GW9662 (20 nM).

(E) Wound-healing assays of control and ACAT1-knockout PC3 cells treated with vehicle or GW9662 (20 nM) over 24 h. Cells were pretreated with GW9662 for 24 h before initiation of the assay. Gap closure was calculated as the difference between the gap areas at 0 and 24 h. Representative images are shown at ×4 magnification. Scale bars, 500 μm.

Fig. 7. Proposed model of ACAT1-dependent SOX4 maintenance and lipid homeostasis in ERG-negative prostate cancer cells.

ACAT1 maintains basal and TNFα-induced SOX4 protein abundance and supports lipid homeostasis, AKT signaling, proliferation, and migration. ACAT1 depletion reduces SOX4 abundance and increases PPARγ abundance, accompanied by neutral lipid accumulation and remodeling of ceramides, DGs, TGs, and PUFA-containing phospholipids. These changes are associated with reduced AKT Ser473 phosphorylation and suppressed proliferation. Extracellular lipid restriction and PPARγ antagonism with GW9662 attenuate lipid accumulation and partially restore signaling and proliferation, whereas GW9662 does not significantly restore gap closure. Dashed connections indicate relationships attenuated following ACAT1 depletion.

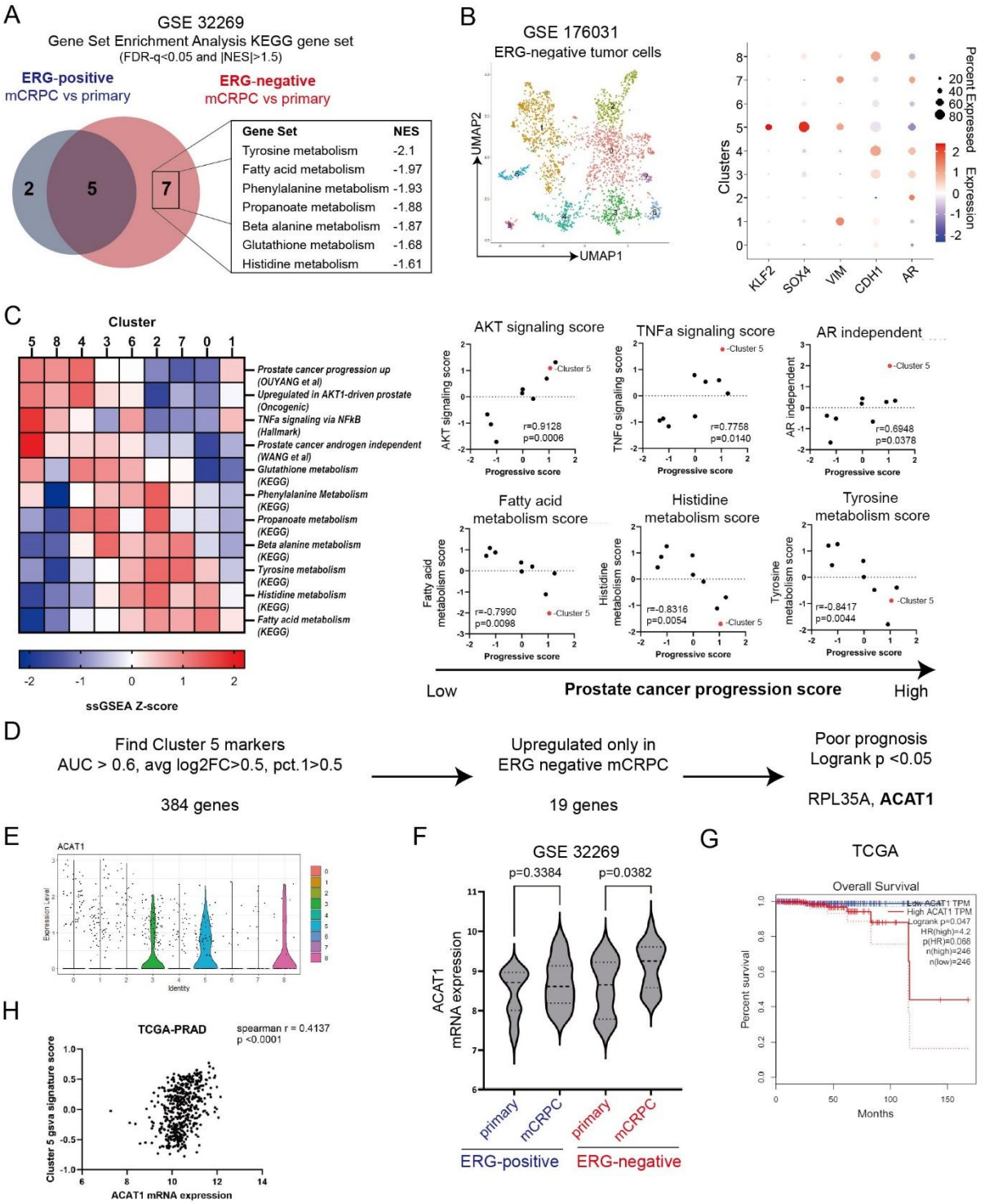

A
GSE 32269
Gene Set Enrichment Analysis KEGG gene set
(FDR-q<0.05 and |NES|>1.5)
ERG-positive
mCRPC vs primary
ERG-negative
mCRPC vs primary
2
5
7
Gene Set NES
Tyrosine metabolism -2.1
Fatty acid metabolism -1.97
Phenylalanine metabolism -1.93
Propanoate metabolism -1.88
Beta alanine metabolism -1.87
Glutathione metabolism -1.68
Histidine metabolism -1.61
B
GSE 176031
ERG-negative tumor cells
UMAP2
UMAP1
Clusters
KLF2
SOX4
VIM
CDH1
AR
Percent Expressed
Expression
C
Cluster
5 8 4 3 6 2 7 0 1
Prostate cancer progression up (OUYANG et al)
Upregulated in AKT1-driven prostate (Oncogenic)
TNFa signaling via NFkB (Hallmark)
Prostate cancer androgen independent (WANG et al)
Glutathione metabolism (KEGG)
Phenylalanine Metabolism (KEGG)
Propanoate metabolism (KEGG)
Beta alanine metabolism (KEGG)
Tyrosine metabolism (KEGG)
Histidine metabolism (KEGG)
Fatty acid metabolism (KEGG)
ssGSEA Z-score
AKT signaling score
TNFa signaling score
AR independent
Fatty acid metabolism score
Histidine metabolism score
Tyrosine metabolism score
Cluster 5
r=0.9128
p=0.0006
r=0.7758
p=0.0140
r=0.6948
p=0.0378
r=-0.7990
p=0.0098
r=-0.8316
p=0.0054
r=-0.8417
p=0.0044
Progressive score
Low
Prostate cancer progression score
High
D
Find Cluster 5 markers
AUC > 0.6, avg log2FC>0.5, pct.1>0.5
384 genes
Upregulated only in
ERG negative mCRPC
19 genes
Poor prognosis
Logrank p <0.05
RPL35A, ACAT1
E
ACAT1
Expression Level
Identity
F
GSE 32269
p=0.3384
p=0.0382
ACAT1
mRNA expression
primary
mCRPC
primary
mCRPC
ERG-positive
ERG-negative
G
TCGA
Overall Survival
Low ACAT1 TPM
High ACAT1 TPM
Logrank p=0.047
HR(high)=4.2
p(HR)=0.068
n(high)=246
n(low)=246
Percent survival
Months
H
TCGA-PRAD
spearman r = 0.4137
p <0.0001
Cluster 5 gsva signature score
ACAT1 mRNA expression

Figure 1

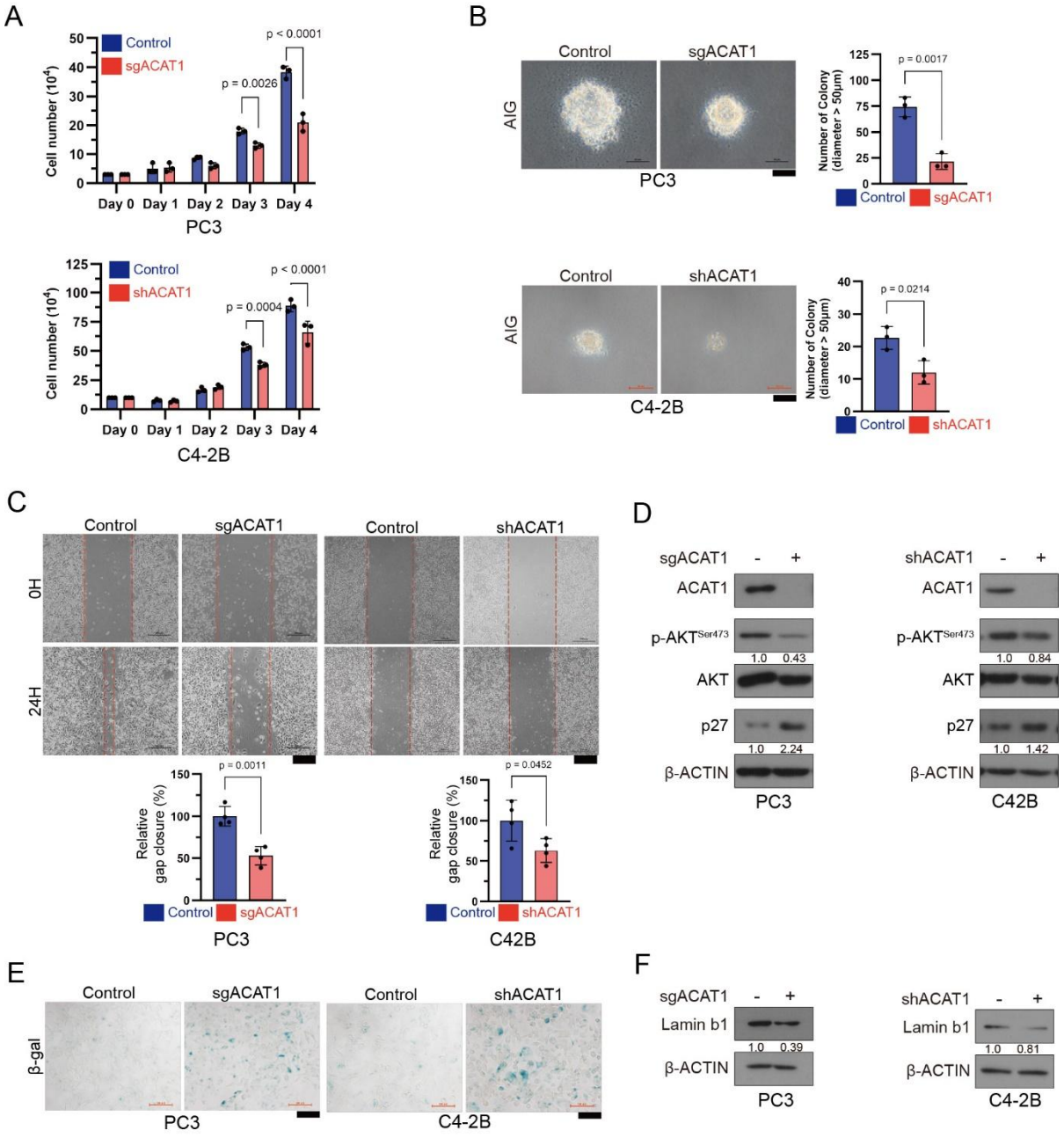

A
Control
sgACAT1
p < 0.0001
p = 0.0026
Cell number (10⁴)
Day 0 Day 1 Day 2 Day 3 Day 4
PC3
Control
shACAT1
p < 0.0001
p = 0.0004
Cell number (10⁴)
Day 0 Day 1 Day 2 Day 3 Day 4
C4-2B
B
Control
sgACAT1
AIG
PC3
p = 0.0017
Number of Colony (diameter > 50μm)
Control sgACAT1
Control
shACAT1
AIG
C4-2B
p = 0.0214
Number of Colony (diameter > 50μm)
Control shACAT1
C
Control
sgACAT1
Control
shACAT1
0H
24H
p = 0.0011
Relative gap closure (%)
Control sgACAT1
PC3
p = 0.0452
Relative gap closure (%)
Control shACAT1
C42B
D
sgACAT1 - +
ACAT1
p-AKTSer473
1.0 0.43
AKT
p27
1.0 2.24
β-ACTIN
PC3
shACAT1 - +
ACAT1
p-AKTSer473
1.0 0.84
AKT
p27
1.0 1.42
β-ACTIN
C42B
E
Control
sgACAT1
Control
shACAT1
β-gal
PC3
C4-2B
F
sgACAT1 - +
Lamin b1
1.0 0.39
β-ACTIN
PC3
shACAT1 - +
Lamin b1
1.0 0.81
β-ACTIN
C4-2B

Figure 2

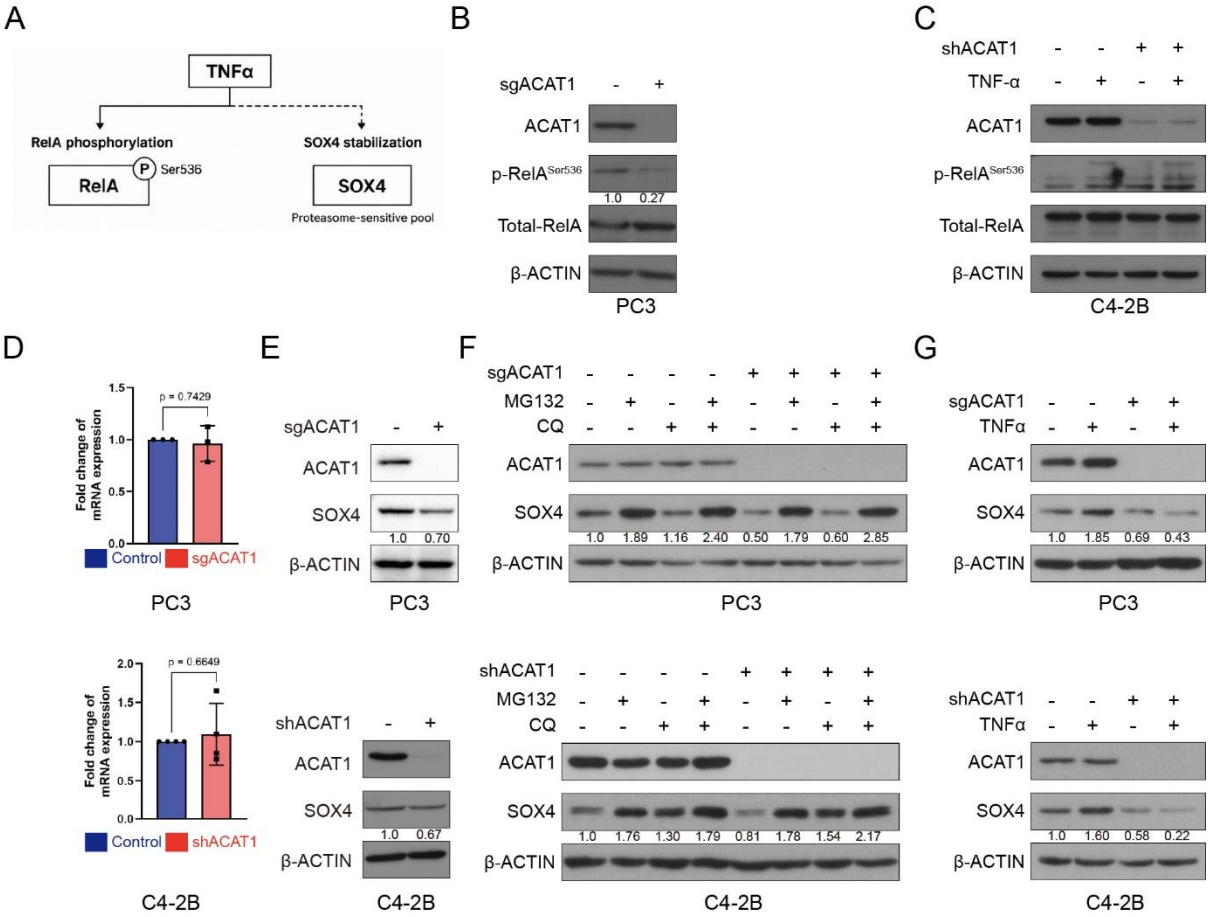

A
TNFα
RelA phosphorylation
SOX4 stabilization
RelA
P Ser536
SOX4
Proteasome-sensitive pool
B
sgACAT1 - +
ACAT1
p-RelA Ser536
1.0 0.27
Total-RelA
β-ACTIN
PC3
C
shACAT1 - - + +
TNF-α - + - +
ACAT1
p-RelA Ser536
Total-RelA
β-ACTIN
C4-2B
D
p = 0.7429
Fold change of mRNA expression
1.5
1.0
0.5
0.0
Control
sgACAT1
PC3
p = 0.6649
Fold change of mRNA expression
2.0
1.5
1.0
0.5
0.0
Control
shACAT1
C4-2B
E
sgACAT1 - +
ACAT1
SOX4
1.0 0.70
β-ACTIN
PC3
shACAT1 - +
ACAT1
SOX4
1.0 0.67
β-ACTIN
C4-2B
F
sgACAT1 - - - - + + + +
MG132 - + - + - + - +
CQ - - + + - - + +
ACAT1
SOX4
1.0 1.89 1.16 2.40 0.50 1.79 0.60 2.85
β-ACTIN
PC3
shACAT1 - - - - + + + +
MG132 - + - + - + - +
CQ - - + + - - + +
ACAT1
SOX4
1.0 1.76 1.30 1.79 0.81 1.78 1.54 2.17
β-ACTIN
C4-2B
G
sgACAT1 - - + +
TNFα - + - +
ACAT1
SOX4
1.0 1.85 0.69 0.43
β-ACTIN
PC3
shACAT1 - - + +
TNFα - + - +
ACAT1
SOX4
1.0 1.60 0.58 0.22
β-ACTIN
C4-2B

Figure 3

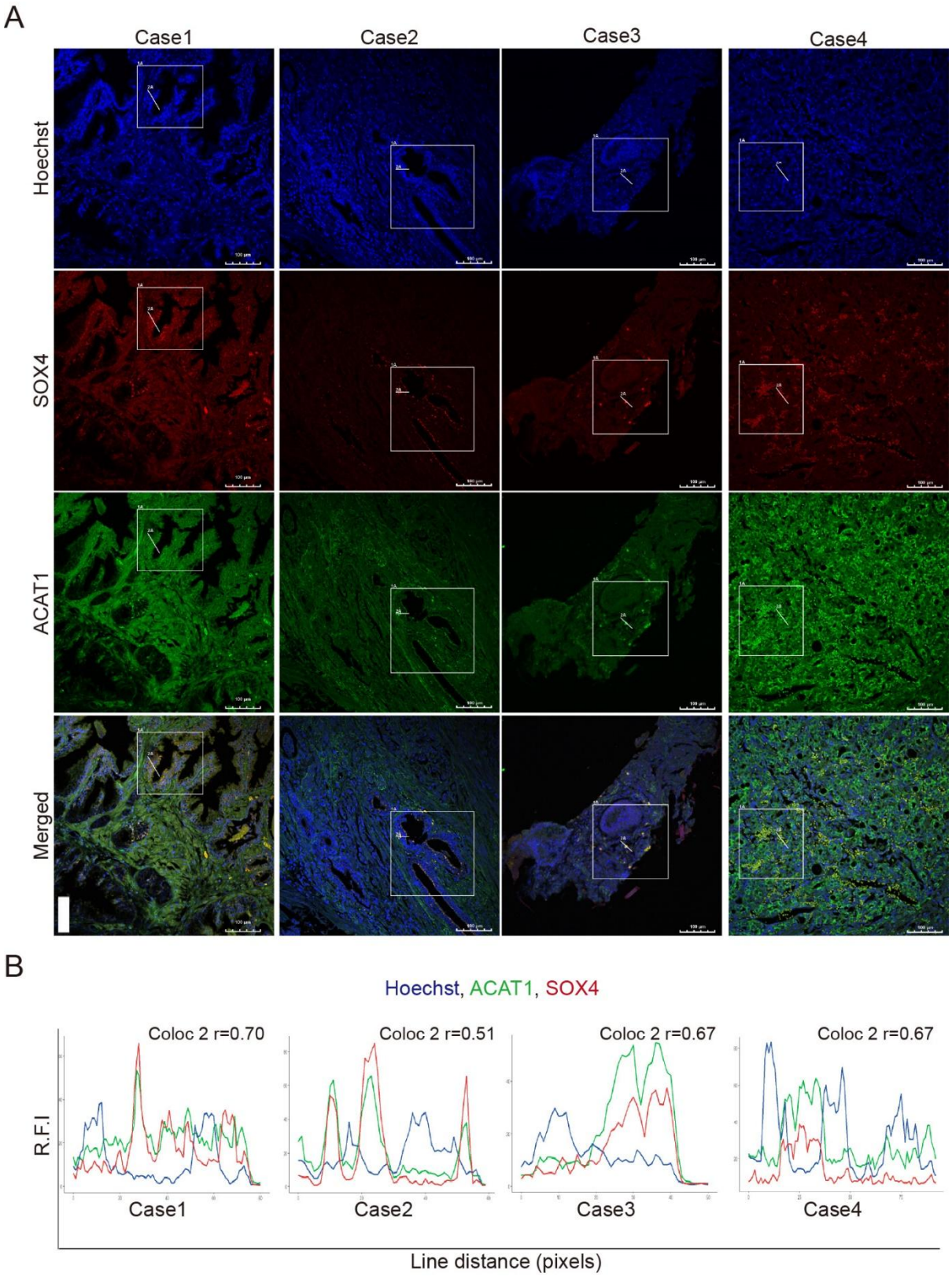

A
Case1
Case2
Case3
Case4
Hoechst
SOX4
ACAT1
Merged
B
Hoechst, ACAT1, SOX4
Coloc 2 r=0.70
Coloc 2 r=0.51
Coloc 2 r=0.67
Coloc 2 r=0.67
R.F.I
Case1
Case2
Case3
Case4
Line distance (pixels)

Figure 4

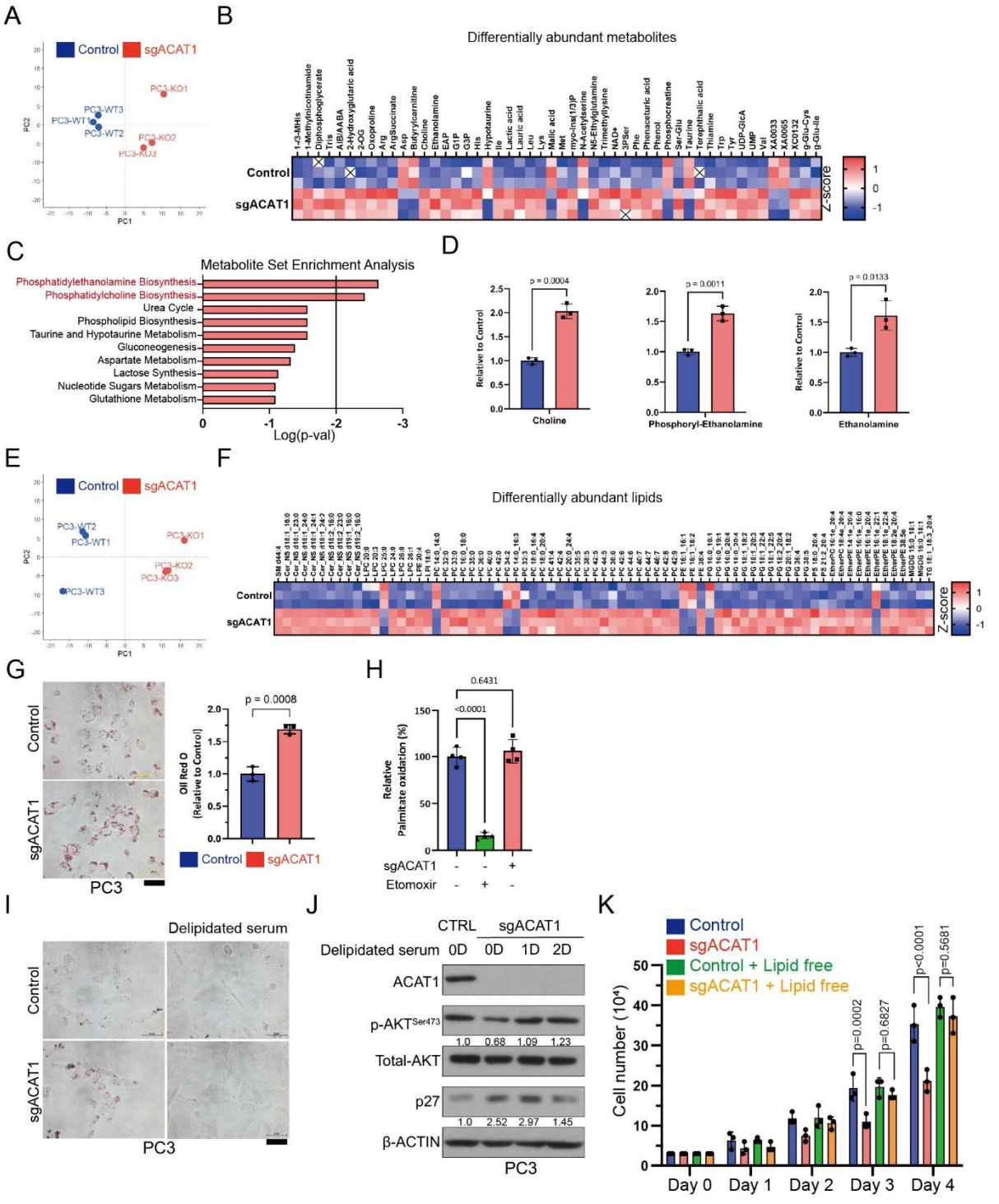

A
Control
sgACAT1
PC3-KO1
PC3-WT3
PC3-WT1
PC3-WT2
PC3-KO2
PC3-KO3
PC1
PC2
B
Differentially abundant metabolites
Control
sgACAT1
Z-score
C
Metabolite Set Enrichment Analysis
Phosphatidylethanolamine Biosynthesis
Phosphatidylcholine Biosynthesis
Urea Cycle
Phospholipid Biosynthesis
Taurine and Hypotaurine Metabolism
Gluconeogenesis
Aspartate Metabolism
Lactose Synthesis
Nucleotide Sugars Metabolism
Glutathione Metabolism
Log(p-val)
D
p = 0.0004
Relative to Control
Choline
p = 0.0011
Phosphoryl-Ethanolamine
p = 0.0133
Relative to Control
Ethanolamine
E
Control
sgACAT1
PC3-WT2
PC3-WT1
PC3-KO1
PC3-KO2
PC3-KO3
PC3-WT3
PC1
PC2
F
Differentially abundant lipids
Control
sgACAT1
Z-score
G
Control
sgACAT1
PC3
p = 0.0008
Oil Red O
(Relative to Control)
Control
sgACAT1
H
0.6431
<0.0001
Relative
Palmitate oxidation (%)
sgACAT1
Etomoxir
I
Delipidated serum
Control
sgACAT1
PC3
J
CTRL
sgACAT1
Delipidated serum 0D 0D 1D 2D
ACAT1
p-AKTSer473
1.0 0.68 1.09 1.23
Total-AKT
p27
1.0 2.52 2.97 1.45
β-ACTIN
PC3
K
Control
sgACAT1
Control + Lipid free
sgACAT1 + Lipid free
Cell number (10⁴)
p=0.0002
p=0.6827
p<0.0001
p=0.5681
Day 0
Day 1
Day 2
Day 3
Day 4

Figure 6

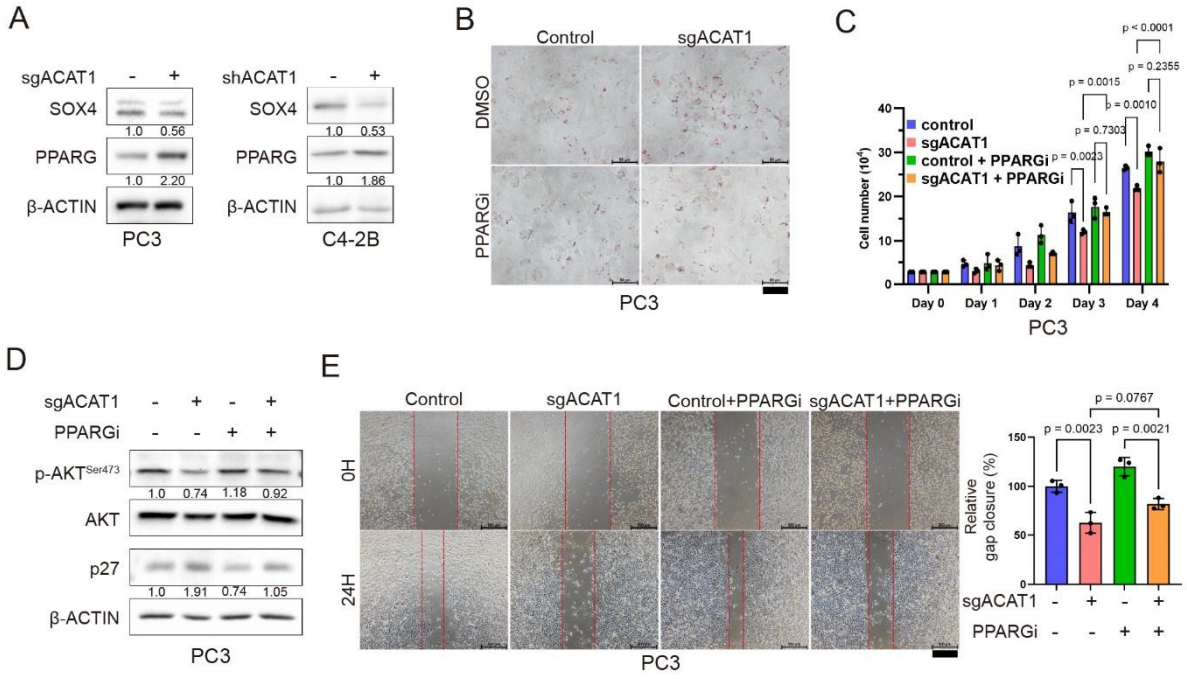

A
sgACAT1 - +
SOX4
1.0 0.56
PPARG
1.0 2.20
β-ACTIN
PC3
shACAT1 - +
SOX4
1.0 0.53
PPARG
1.0 1.86
β-ACTIN
C4-2B
B
Control
sgACAT1
DMSO
PPARGi
PC3
C
p < 0.0001
p = 0.2355
p = 0.0015
p = 0.0010
p = 0.7303
p = 0.0023
control
sgACAT1
control + PPARGi
sgACAT1 + PPARGi
Cell number (10⁴)
Day 0
Day 1
Day 2
Day 3
Day 4
PC3
D
sgACAT1 - + - +
PPARGi - - + +
p-AKT Ser473
1.0 0.74 1.18 0.92
AKT
p27
1.0 1.91 0.74 1.05
β-ACTIN
PC3
E
Control
sgACAT1
Control+PPARGi
sgACAT1+PPARGi
0H
24H
PC3
p = 0.0767
p = 0.0023
p = 0.0021
Relative gap closure (%)
sgACAT1 - + - +
PPARGi - - + +

Figure 6

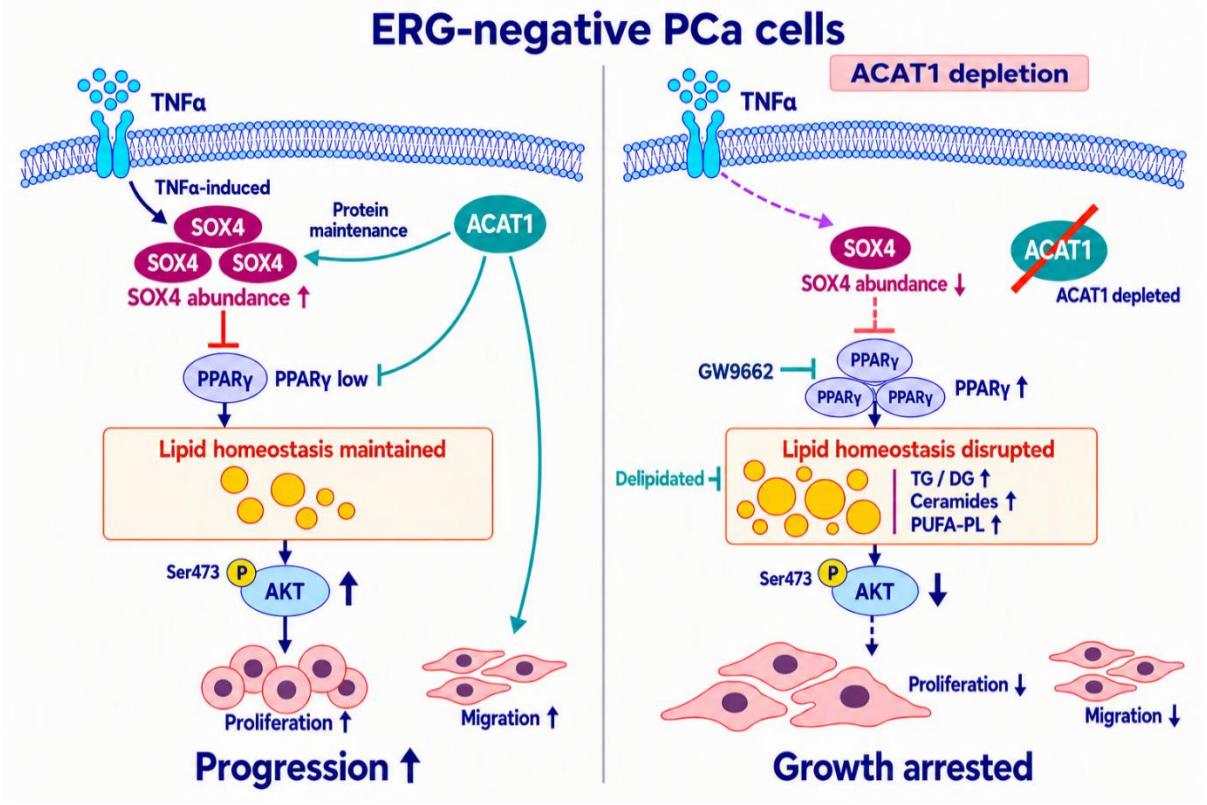

ERG-negative PCa cells
TNFα
TNFα-induced
SOX4
SOX4
SOX4
SOX4 abundance ↑
Protein maintenance
ACAT1
PPARγ
PPARγ low
Lipid homeostasis maintained
Ser473
P
AKT
Proliferation ↑
Migration ↑
Progression ↑
ACAT1 depletion
TNFα
SOX4
SOX4 abundance ↓
ACAT1
ACAT1 depleted
GW9662
PPARγ
PPARγ
PPARγ
PPARγ ↑
Delipidated
Lipid homeostasis disrupted
TG / DG ↑
Ceramides ↑
PUFA-PL ↑
Ser473
P
AKT
Proliferation ↓
Migration ↓
Growth arrested

Figure 7

Supplementary Files

This is a list of supplementary files associated with this preprint. Click to download.

- AdditionalFile1SupplementaryTableS1.xlsx
- AdditionalFile2SupplementaryTableS2.xlsx
- AdditionalFile3SupplementaryTableS3.xlsx
- AdditionalFile4SupplementaryTableS4.xlsx
- AdditionalFile5SupplementaryTableS5.xlsx
- AdditionalFile6SupplementaryFigures.docx
- AdditionalFile7Uncroppedblots.pdf
- AdditionalFile8Materialsfinal.xlsx
- SupplementaryFigure1highresolution.tif
- SupplementaryFigure2highresolution.tif
- SupplementaryFigure3highresolution.tif
- SupplementaryFigure4highresolution.tif
- SupplementaryFigure5highresolution.tif
- SupplementaryFigure6highresolution.tif
- SupplementaryFigure7highresolution.tif